13

Deconvolution of Long-Pulse Lidar Profiles

Ljuan L. Gurdev, Tanja N. Dreischuh
and Dimitar V. Stoyanov
Institute of Electronics, Bulgarian Academy of Sciences 72, Tzarigradsko shosse, Sofia Bulgaria

1. Introduction

Active remote-sensing methods and instruments such as microwave radars, optical radars (lidars), and acoustical radars (sodars, sonars) have widely been used for in-depth or surface probing of atmosphere, ocean and earth (Doviak & Zrnic, 1984; Measures, 1984; Kovalev & Eichinger, 2004; Van Trees, 2001; Marzano & Visconti, 2002). The recent active sensing methods are based mainly on the so-called lidar (LIght Detection And Ranging) or Time-Of-Flight (TOF) principle (Measures, 1984; Kovalev & Eichinger, 2004). This principle consists in the detection of backscattering-due radiative returns (at angle π) from the probed media after irradiating them by penetrating narrow-beam pulsed radiation. Then, the return signal profile detected in the time domain contains range-resolved information about the radiation-matter interaction (absorption and scattering) processes and the related material characteristics along the line of sight (LOS). The range-resolution scale (along the LOS) is determined by the (larger of the) characteristic pulse response length and the sampling interval $\Delta z_0 = c\Delta t_0/2$ of the lidar system, and by the noise level and bandwidth (Gurdev et al., 1998, 1993); Δt_0 is the sampling interval (the digitizing step) in the time domain. The value of Δz_0 is usually assumed to be less than the least variation scale of the investigated extinction and backscattering inhomogeneities.

Thus, a "hardware" way of improving the accuracy and resolution of lidars is to use as fast as possible analog-to-digital converters (ADC) and as short as possible sensing laser pulses. Consequently, the realization of the hardware approach depends on the development of the electronic and laser technologies and is connected with overcoming different technological difficulties. For instance, shortening the laser pulses is often connected with lowering the pulse energy or increasing the (peak) pulse power. Then, in the former case one should amplify the shortened pulses while in the latter case the pulse power should be restricted to avoid nonlinear disturbance of the investigated (sensed) medium. Let us also note that in coherent heterodyne lidars the sensing pulse length should be above a threshold determined by the required resolution of measuring the Doppler velocity and the wavelength of the sensing radiation (Hannon & Thomson, 1994). The only way of improving the range resolution in this case is to use shorter laser pulses of proportionally shorter radiation wavelength. As another example one may consider GRAYDAR (Gamma RAY Detection

And Ranging) (Gurdev et al., 2007a, 2007b; Dreischuh et al., 2007) where, because of the absence of short-pulse gamma ray lasers, the δ–pulse sensing procedure is based on the use of electron-positron annihilation-due gamma-photon pairs.

At the same time, there exist some "software" approaches to improving the resolution and accuracy of the lidars. One of them consists in the use of deconvolution techniques (algorithms) for recovering the short-pulse lidar profiles on the basis of the measured long-pulse lidar profiles and known sensing pulse shape (Gurdev et al., 1993, 1998; Dreischuh et al., 1995, 1996; Stoyanov et al., 1996; Park et al., 1997; Bahrampour & Askari, 2006). Specific approaches have also been developed to improving the resolution of coherent heterodyne pulsed Doppler lidars (Gurdev et al., 2001, 2002, 2003, 2008a). Mention as well an original and effective approach to achieving lidar-signal sampling intervals shorter than the data acquisition step based on the random delay of the sensing laser shots with respect to the ADC start pulses (Stoyanov et al., 2004, 2007, 2010).

The purpose of the present chapter is to give a brief review of the works and to generalize the results obtained there about the advantages and limitations of some above-mentioned software approaches to improving the resolution and the accuracy of different TOF-based (lidar type) sensing methods. The first circle of problems considered is devoted mainly to deconvolution techniques for improving the resolution of long-pulse elastic lidars for sensing the atmosphere. The features are marked of Fourier and Volterra deconvolution algorithms at different levels and types of the measurement noise, and different types of uncertainties of the sensing laser pulses. The well-defined pulses of special concrete shape obtained by pulse-shaping are also of interest because they allow the design of special effective deconvolution algorithms. Here we also briefly describe a double-sided linear-strategy variant of lidar-type optical tomography. The following topic of interest concerns a novel (center-of-mass wavelength) Thomson scattering lidar method for measuring electron temperature profiles in thermonuclear plasmas (Gurdev et al., 2008b; Dreischuh et al., 2009) as well as some recent results about the Fourier-deconvolution due improvement of the sensing accuracy and resolution in this case. The concluding part of the chapter contains a brief discussion of the investigations described and the results obtained as well as of the importance of the software approaches to improving the lidar sensing accuracy and resolution.

2. Lidar equations

Let us consider a material object irradiated by penetrating quasi-monochromatic narrow-beam pulsed radiation of wavelength λ_i (Fig.1). The direct detection of the backscattering-due radiative return transforms it into an electrical signal (return signal) F measured as a function of the time delay t after the instant of pulse emission. In this way a temporal return signal profile $F(t)$ is obtained. At practically constant speed of propagation c of the sensing radiation and single-scattering conditions, there exists one-to-one correspondence $t \equiv 2z/c$ ($z \equiv ct/2$) between the time t and the LOS distance z to the sensing-pulse front that is in fact the front of the scattering volume contributing to the signal at this time (Measures, 1984; Kovalev & Eichinger, 2004). Then, one can write that $F=F(t=2z/c)=F(z=ct/2)$, which is an expression of the basic feature of the lidar (or TOF) principle. That is, the return signal profile in the time domain contains range-resolved information about the radiation-matter interaction (absorption and scattering) processes and the related material characteristics along the LOS.

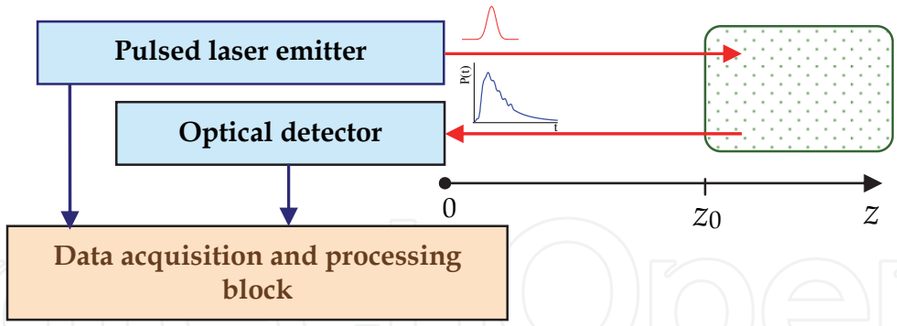

Fig. 1. Illustration of the lidar principle.

In the general case of inelastic scattering and presence of broadening effects, the lidar return will be frequency shifted and spectrally broadened. Then, the detected return power $P_l(\lambda_{s1},\lambda_{s2};z=ct/2)$ within a wavelength interval $[\lambda_{s1},\lambda_{s2}]$ is given by the following most general lidar equation (e.g. Measures, 1984; Gurdev et al., 2008b, 1998):

$$P_l(\lambda_{s1},\lambda_{s2};z) = AE_0(\lambda_i)\int_{\lambda_{s1}}^{\lambda_{s2}} d\lambda_s K(\lambda_i,\lambda_s)\int_0^z dz' f[2(z-z')/c]\Phi(\lambda_i,\lambda_s;z'), \quad (1)$$

where A is the lidar receiving aperture area, $E_0(\lambda_i)$ is the incident (sensing) pulse energy, $K(\lambda_i, \lambda_s)$ is a characteristic of the transceiving spectral transparency and sensitivity of the lidar, $f(\theta)$ is the effective pulse response function of the lidar system, θ is time variable,

$$\Phi(\lambda_i,\lambda_s;z) = \eta(\lambda_i,\lambda_s;z)\beta(\lambda_i;z)L(\lambda_i,\lambda_s;z)T(\lambda_i,\lambda_s;z)/z^2 , \quad (2)$$

η is receiving efficiency of the lidar, λ_i and λ_s are wavelengths of the incident and the backscattered radiation, respectively, β is the volume backscattering coefficient, $L(\lambda_i,\lambda_s;z)$ is the spectral contour of the scattered radiation,

$$T(\lambda_i,\lambda_s;z) = \exp\left\{-\int_0^z [\alpha_t(\lambda_i,z')+\alpha_t(\lambda_s,z')]dz'\right\} \quad (3)$$

is the two-way transparency of the investigated medium (from $z'=0$ to $z'=z$), and $\alpha_t(\lambda_i, z')$ and $\alpha_t(\lambda_s, z')$ are respectively the forward and backward extinction coefficients.
When the system response length [concerning $f(\theta)$] is less than the least variation scale of the properties of the medium, Eq.(1) is reduced to the following (short-pulse, δ-pulse, or maximum-resolved, Gurdev et al., 1993) lidar equation:

$$P_s(\lambda_{s1},\lambda_{s2};z) = \frac{cA}{2}E_0(\lambda_i)\int_{\lambda_{s1}}^{\lambda_{s2}} d\lambda_s K(\lambda_i,\lambda_s)\Phi(\lambda_i,\lambda_s;z). \quad (4)$$

At last, in the case of a single line shape $L(\lambda_s)$ that is essentially narrower than the dependence of K on λ_s, instead of the long-pulse and short-pulse Eqs.(1) and (4), respectively, we obtain

$$P_l(\lambda_{sc};z) = AE_0(\lambda_i)K(\lambda_i,\lambda_{sc})\int_0^z dz' f[2(z-z')/c]\Phi(\lambda_i,\lambda_{sc};z') \quad (5)$$

and

$$P_s(\lambda_{sc};z)=\frac{cA}{2}E_0(\lambda_i)K(\lambda_i,\lambda_{sc})\Phi(\lambda_i,\lambda_{sc};z)\,, \tag{6}$$

where λ_{sc} is the central wavelength of $L(\lambda_s)$ and

$$\Phi(\lambda_i,\lambda_{sc};z)=\eta(\lambda_i,\lambda_{sc};z)\beta(\lambda_i;z)T(\lambda_i,\lambda_{sc};z)/z^2\ . \tag{7}$$

In case of elastic scattering, $\lambda_{sc}=\lambda_i$. Let us also note that the effective pulse response function of the lidar, $f(\theta)$, is a convolution

$$f(\theta)=\int_{-\infty}^{\infty}d\theta' q(\theta-\theta')s(\theta') \tag{8}$$

of the receiving-system (including the ADC unit) pulse response $q(\theta)$ ($\int_0^{\infty}q(\theta)d\theta=1$) and the sensing-pulse shape $s(\theta)=P_p(\theta)/E_0$, where $P_p(\theta)$ is the pulse power shape.
The above-described lidar equations are basic instruments for quantitative analysis of data obtained by direct-detection lidars. They are adaptable to photon-counting mode of detection by using the formal substitutions:

$$P_l\rightarrow N_l\,,\quad P_s\rightarrow N_s,\quad E_0\rightarrow N_0,\quad L(\lambda_s)\rightarrow L(\lambda_s)\,\lambda_s/\lambda_i\ , \tag{9}$$

where N_l and N_s are photon counting rates, and N_0 is the number of photons in the incident laser pulse.

3. Deconvolution techniques for improving the resolution of long-pulse direct-detection elastic lidars

In the case of elastic, e.g., aerosol or Rayleigh scattering in the atmosphere, the lidar return is characterized by too small spectral broadening and is described in general by Eq.(5) at $\lambda_{sc}=\lambda_i$. Instead of Eq.(5), it is convenient to write

$$P_l(z)=(2/c)\int_{\eta}^{\mu}dz' f[2(z-z')/c]P_s(z') \tag{10}$$

For pulse response functions $f(\theta)$ with asymptotically decreasing tails, the integration limits in Eq.(10) may be retained the same as in Eq.(5), that is, $\eta=0$ and $\mu=z$. At the same time, one may choose to write $\eta=-\infty$ and $\mu=\infty$ because the functions $P_l(z)$, $P_s(z)$ and $f(\theta=2z/c)$ are supposed defined and integrable over the interval $(-\infty,\infty)$. The finite integration limits $\eta=0$ and $\mu=z$ indicate only the points where the integrand becomes identical to zero. When the response function is restricted, say rectangular, with duration τ, the integration limits are $\eta=z-c\tau/2$ and $\mu=z$. In any case, the software approach to improving the lidar resolution consists in solving the integral equation (10) with respect to the maximum-resolved lidar profile $P_s(z)$ at measured long-pulse profile $P_l(z)$ and measured or estimated system response shape $f(\theta)$.
With $\eta=-\infty$ and $\mu=\infty$, Eq.(10) represents $P_l(z)$ as convolution of $P_s(z)$ and $f(\theta=2z/c)$. Then, the solution with respect to $P_s(z)$ is obtainable in principle by Fourier deconvolution, but attentive noise analysis should be performed and noise-suppressing techniques should be used to ensure satisfactory recovery accuracy. When the spectral density $I_f(\omega)$ of $f(\theta)$ has

zeros or is considerably narrower than the spectral density $I_n(\omega)$ of the noise (see below), the Fourier deconvolution becomes impracticable and Eq.(10), with η=0 and μ=z, could be considered and solved as the first kind of Volterra integral equation with respect to $P_s(z)$. The retrieval of $P_s(z)$ for some special, e.g., rectangular, rectangular-like or exponentially-shaped response functions can also be performed analytically at relatively low and controllable noise influence.

Eq.(10) can naturally be given in a discrete form based on sampling the signal and the lidar response function. Then, the solution with respect to $P_s(z)$ is obtainable by using matrix formulation of the problem (Park et al., 1997). Other deconvolution techniques such as Fourier-based regularized deconvolution, wavelet-vaguelette deconvolution and wavelet denoising, and Fourier-wavelet regularized deconvolution can also be effective in this case (Bahrampour & Askari, 2006; Johnstone et al., 2004). A retrieval of the maximum-resolved lidar profile with improved accuracy and resolution is achievable as well using iterative deconvolution procedures (Stoyanov et al., 2000; Refaat et al., 2008). Note by the way that the applied problems concerning deconvolution give rise to a powerful development of the mathematical theory of deconvolution (e.g., Pensky and Sapatinas, 2009, 2010).

Below we shall describe an extended, more complete analysis, in comparison with our former works, of the above-mentioned general (Fourier and Volterra) and special (for concrete response functions) deconvolution approaches. The fact will be taken into account that the signal-induced (say Poisson or shot) noise or the background-due noise is smoothed by the lidar response function. Let us first consider some features of the Fourier-deconvolution procedure. Suppose in general that the noise N accompanying the signal $P_s(z)$ consists of two components, N_1 and N_2, where N_1 is induced by the signal itself, and N_2 is a stationary background independent of the signal. Then the measured lidar profile to be processed is

$$P_{lm}(z) = P_l(z) + (2/c)\int_{-\infty}^{\infty} dz'\{f[2(z-z')/c]N_1(z') + q[2(z-z')/c]N_2(z')\} . \quad (11)$$

The Fourier deconvolution based on Eq.(10), with $P_{lm}(z)$ [Eq.(11)] instead of $P_l(z)$, is straightforward and leads to the following expression of the restored profile $P_{sr}(z)$:

$$P_{sr}(z) = (2\pi)^{-1}\int_{-\infty}^{\infty} \tilde{P}_s(k)\exp(-jkz)dk + \varepsilon(z) = (2\pi)^{-1}\int_{-\infty}^{\infty} [\tilde{P}_l(k)/\tilde{f}(\omega)]\exp(-jkz)dk + \varepsilon(z) , \quad (12)$$

where ω=ck/2, j is imaginery unity, t=2z/c,

$$\tilde{P}_l(k) = \int_{-\infty}^{\infty} P_l(z)\exp(jkz)dz , \ \tilde{f}(\omega) = \int_{-\infty}^{\infty} f(t)\exp(j\omega t)dt , \text{ and } \tilde{P}_s(k) = \int_{-\infty}^{\infty} P_s(z)\exp(jkz)dz \quad (13)$$

are respectively Fourier transforms of $P_l(z)$, $f(t)$, and $P_s(z)$, and

$$\varepsilon(z) = N_1(z) + (2\pi)^{-1}\int_{-\infty}^{\infty} [\tilde{N}_2(k)\tilde{s}(\omega)]\exp(-jkz)dk \quad (14)$$

is a formally written realization of the random error due to the noise;

$$\tilde{N}_2(k) = \int_{-z_l}^{z_l} N_2(z)\exp(jkz)dz , \quad \tilde{s}(\omega) = \int_{-\infty}^{\infty} s(t)\exp(j\omega t)dt , \quad (15)$$

and $[-z_l,z_l]$ is the real integration interval instead of $[-\infty,\infty]$ supposed to be sufficiently large that $P_s(z)$ is fully restored to some characteristic distance $z_c<z_l$ for which $P_s(z_c)$ practically vanishes. Assuming that the correlation radius r_{c2} of $N_2(z)$ is much smaller than z_l and using Eqs.(14) and (15), we obtain (in the limit $z_l\to\infty$) the following expression for the error variance:

$$D\varepsilon(z)=\left\langle \varepsilon^2(z)\right\rangle = D_{N_1}(z)+(2\pi)^{-1}\int_{-\infty}^{\infty}[I_{N_2}(k)/I_s(\omega)]dk\,, \tag{16}$$

where, respectively, $I_s(\omega)=|s(\omega)|^2$ and $I_{N_2}(k)=\lim_{z_l\to\infty} D_{N_2}\int_{-2z_l}^{2z_l} K_{N_2}(\zeta)\exp(jk\zeta)d\zeta$ are spectral densities of $s(t)$ and $N_2(z)$, and $D_{N_1}(z)=<N_1^2(z)>$ and $D_{N_2}=<N_2^2(z)>$ are variances of $N_1(z)$ and $N_2(z)$; $K_{N_2}(\zeta)=\left\langle N_2(z)N_2(z+\zeta)\right\rangle / D_{N_2}$ is the correlation coefficient of $N_2(z)$, and <.> denotes an ensemble average. According to Eq.(16), when the noise spectrum $I_{N_2}(k)$ is wider than $I_s(\omega=ck/2)$, the variance $D\varepsilon$ would have infinite value. Consequently, some type of low-pass filtering is always necessary for decreasing the noise influence, retaining an improved retrieval resolution.

When the measured long-pulse lidar profile $P_{lm}(z)$ is smoothed by a low-pass filter $\varphi(z\text{-}z')$ with spectral characteristic $\tilde{\varphi}(k)=\int_{-\infty}^{\infty}\varphi(z)\exp(jkz)dz$, Eqs.(12), (14), and (16) retain their forms, where only the following substitutions should be introduced

$$\tilde{P}_l(k)\to\tilde{P}_l(k)\tilde{\varphi}(k)\,;\; N_1(z)\to(2\pi)^{-1}\int_{-\infty}^{\infty}\tilde{N}_1(k)\tilde{\varphi}(k)\exp(-jkz)dk\,;\; \tilde{N}_2(k)\to\tilde{N}_2(k)\tilde{\varphi}(k)\,;$$

$$I_{N_2}(k)\to I_{N_2}(k)|\tilde{\varphi}(k)|^2\,;\; D_{N_1}(z)\to(2\pi)^{-1}\int I_{N_1}(k,z)|\tilde{\varphi}(k)|^2dk\,; \tag{17}$$

where

$$\tilde{N}_1(k)=\int_{-z_l}^{z_l} N_1(z)\exp(jkz)dz\,, \tag{18a}$$

and $N_1(z)$ is assumed to be statistically quasihomogeneous random function (Rytov, 1976) such that its local spectral density and covariance are, respectively,

$$I_{N_1}(k,z)=\lim_{z_l\to\infty}\int_{-2z_l}^{2z_l} Cov(\rho,z)\exp(jk\rho)d\rho\,, \tag{18b}$$

$$Cov(\rho,z)=\left\langle N_1(z+\rho/2)N_1(z-\rho/2)\right\rangle\,. \tag{18c}$$

An improved retrieval resolution may be achieved as well with increasing the computing step $\Delta z=c\Delta t/2$, whose least value $\Delta z_0=c\Delta t_0/2$ is the sampling interval. The finite-computing-step systematic (bias) error depends, in general, on the value of Δz and on the shape of $P_s(z)$ (Gurdev et al., 1993). Naturally, for a lower value of Δz and a smoother shape of $P_s(z)$, the bias error is smaller. In the absence of noise, at short-enough computing step a high accuracy in the restoration of $P_s(z)$ is achievable.

To estimate the effect of a finite computing step on the value of $D\varepsilon$, Eq.(16) should be rewritten as

$$D\varepsilon(z)=D_{N_1}(z)+(2\pi)^{-1}\int_{-\pi/\Delta z}^{\pi/\Delta z}[I_{N_2}(k)/I_s(\omega)]dk\,. \tag{19}$$

According to Eq.(19), when Δz increases above r_{c2}, the effect of the noise decreases because of narrowing its spectral band. When the spectrum $I_{N_2}(k)$ is narrow compared with $I_s(\omega = ck/2)$, i.e., when r_{c2} exceeds the pulse length, from Eq.(19) the lower limit is obtained, $D\varepsilon_{\min} = D_{N_1}(z) + D_{N_2}$, of the variance $D\varepsilon$.

The Fourier-deconvolution systematic retrieval error due to uncertainties in the pulse response function $f(\theta)$ is investigated in depth and detail in Dreischuh et al., 1995. It is shown that various, deterministic or random uncertainties give rise to two main effects on the retrieval accuracy. First, depending on the sign of the uncertainty, an elevation or lowering takes place of the smooth component of the lidar profile. This shift up or down is proportional to the smooth component and to the ratio of the uncertainty area to the true pulse area. The smooth uncertainties affect the whole lidar profile in the same way. The fast varying high-frequency uncertainties lead in addition to amplitude and phase distortions of the small-scale high-frequency structure of the lidar profile. Extremely sharp characteristic-spike cuts and fast-varying alternating-sign (deterministic or random) uncertainties lead to small retrieval errors because of their small areas. The results from investigating the influence of the pulse response uncertainties on the retrieval error allow one to estimate the order and the character of the possible recovery distortions and to choose ways to reduce or prevent them. For instance, in the case of a spike-cut uncertainty in the laser pulse shape, the use of a suitable approximation, instead of the unknown true spike spectrum, leads to effective error reduction (Stoyanov et al., 1996).

In the cases when the Fourier deconvolution becomes impracticable, when for instance the spectrum $I_{N_2}(k)$ is much wider than $I_s(\omega = ck/2)$ or $I_s(\omega)$ has zero spectral components, Eq.(10) can be considered in the form

$$P_l(z) = (2/c)\int_0^z dz' f[2(z-z')/c] P_s(z') \ , \tag{20}$$

which is the first kind of Volterra integral equation. By the substitution $t'=2z'/c$ ($t=2z/c$), and with double differentiation assuming that $f(0)=0$, we obtain

$$P_s(ct/2) = \Im(t) + \int_0^t K(t-t') P_s(ct'/2) dt' \ , \tag{21}$$

where $\Im(t) = P_l^{II}(t = 2z/c)/f^I(0)$, $K(t-t') = -f^{II}(t-t')/f^I(0)$, $f^I(0) = f^I(t-t')|_{t'=t}$, and the symbols such as $\varphi^{J}(y)$ (J = I,II,…) denote the J th derivative of the function φ with respect to y. Eq.(21) is the second kind of Volterra integral equation with respect to $P_s(ct/2=z)$, which has a unique continuous solution within the interval $[t_0, t]$ ($[z_0, z]$, respectively), when $\Im(t)$ is a continuous function within the same interval and the kernel $K(t - t')$ is a continuous or square-summable function of t and t' over some rectangle $\{ t_0 \le t, t' \le \theta \}$. The solution of Eq.(21) is obtainable in the form

$$P_s(ct/2) = \Im(t) + \int_0^t R(\xi)\Im(t-\xi) d\xi \ , \tag{22}$$

where the substitution $t'=t-\xi$ is used meanwhile. Here $R(\xi) = \sum_{i=1}^{\infty} K_i(\xi)$ is the resolvent, $K_i(\xi) = \int_0^{\xi} K_{i-1}(\zeta) K_1(\xi - \zeta) d\zeta$, and $K_1(\xi) = K(\xi)$. The bias error $\delta(z=ct/2) = P_{sc}(z=ct/2) -$

$P_s(z=ct/2)$ caused by the finite calculation step Δt is obtainable by using Eq.(22), provided that the resolvent R is known almost without error as if it is calculated with a computing step much less than Δt. The result is that

$$\delta(z=ct/2)=-(2/30)\Delta t^4[P_s^{IV}(t)-\Im^I(t_0)R^{II}(t-t_0)-\Im^{II}(t_0)R^I(t-t_0)-\Im^{III}(t_0)R(t-t_0)]\,. \quad (23)$$

$P_{sc}(z = ct/2)$ is the numerically restored profile in the absence of noise.

The noise influence on the retrieval accuracy can be estimated taking into account the fact that the noise N_1 is convolved with the overall lidar response function $f(\theta)$, while the noise N_2 is convolved with the receiving system response function $q(\theta)$. Assume that the durations of $f(\theta)$ and $q(\theta)$ are respectively τ_f and τ_q. They are in practice the correlation times of the effective additive noises obtained by the convolution of N_1 and N_2 [see Eq. (11)]. Following the approach employed in Gurdev et al., 1993, the variance $D\varepsilon(z)=<\varepsilon^2(z)>$ of the random error $\varepsilon(z)$ is estimated as

$$D\varepsilon(z)\sim[f^I(0)]^{-2}[D_{N_1}(z)\tau_{c1}/\tau_f^5+D_{N_2}\tau_{c2}/\tau_q^5]\,, \quad (24a)$$

where $\tau_{c1,2}$ (assumed here $<<\tau_f,\tau_q$) are the correlation times of N_1 and N_2, respectively. Because of the real discrete calculation procedure the computing step Δt plays in fact the role of minimum correlation time with respect to N_1 and N_2 and their convolutions with the corresponding response functions [Eq. (11)]. In this case, when $\tau_{f,q}<\Delta t$

$$D\varepsilon(z)\sim[f^I(0)]^{-2}[D_{N_1}(z)+D_{N_2}](\Delta t)^{-4}\ . \quad (24b)$$

In the opposite case, when $\tau_{c1,2}>>\tau_f,\tau_q>\Delta t$, it is obtained that

$$D\varepsilon(z)\sim[f^I(0)]^{-2}[D_{N_1}(z)/\tau_{c1}^4+D_{N_2}/\tau_{c2}^4]\ . \quad (24c)$$

According to Eqs.24a-c, as in the case of Fourier deconvolution, a fast fluctuating broadband noise leads to higher statistical deconvolution error compared to a slowly fluctuating narrowband noise whose effect is lowered by the deconvolution.

The sensing laser pulse shape conditions entirely the processes of convolution and deconvolution when its duration $\tau_s>>\tau_q$. Such is for instance the case of atmospheric lidars, where the receiving system response time τ_q is substantially less than the laser pulse duration τ_s and practically $f(\theta)\equiv s(\theta)$. There are some types of laser pulse shapes in this case that lead to simple, accurate and fast deconvolution algorithms permitting one by suitable scanning to investigate in real time the fine spatial structure of atmosphere or other objects penetrated by the sensing radiation. Such pulses are the so-called rectangular, rectangular-like, and exponentially-shaped pulses to which it is impossible or difficult to apply Fourier or Volterra deconvolution techniques. The contemporary progress in the pulse shaping art would allow one to obtain various desirable laser pulse shapes.

In the case of rectangular laser pulses with duration τ, when $f(\theta)=\tau^{-1}$ for $\theta\in[0,\tau]$ and $f(\theta)=0$ for $\theta\notin[0,\tau]$, Eq.(10) acquires the form

$$P_l(z)=(2/c\tau)\int_{z-c\tau/2}^{z}dz'P_s(z')\ . \quad (25)$$

The differentiation of Eq.(25) leads to the relation

$$P_s(z) = (c\tau / 2)P_l^I(z) + P_s(z - c\tau / 2) \quad , \tag{26}$$

that is,

$$P_s(z) = (c\tau / 2)\sum_{i=1}^{Q} P_l^I(z - ic\tau / 2) + P_s(z - (Q+1)c\tau / 2) \ , \tag{27}$$

where Q is the integer part of t/τ=$2z/c\tau$. The distortion $\delta(z=ct/2)$ caused by a finite computing step $\Delta z=c\Delta t/2$ is estimated on the basis of Eq.(26) as

$$\delta(z) = -(1/30)(\Delta z)^4 P_s^{\mathrm{IV}}(z) \quad . \tag{28}$$

On the basis of Eqs.(11) and (27), the variance $D\varepsilon(z)=<\varepsilon^2(z)>$ of the random rectangular-pulse deconvolution error $\varepsilon(z)$ is estimated as

$$D\varepsilon(z) \sim \tau^2(Q+1)[D_{N_1}(z)\tau_{c1} / \tau_f^3 + D_{N_2}\tau_{c2} / \tau_q^3] \, , \tag{29a}$$

when $\tau_{c1,2} << \tau_{f,q}$, and

$$D\varepsilon(z) \sim \tau^2(Q+1)[D_{N_1}(z)\tau_{c1}^{-2} + D_{N_2}\tau_{c2}^{-2}] \, , \tag{29b}$$

when $\tau_{c1,2} >> \tau_{f,q}$; $\tau_f \equiv \tau$. When $\tau_{f,q} < \Delta t$, instead of (29a) we have

$$D\varepsilon(z) \sim \tau^2(Q+1)[D_{N_1}(z) + D_{N_2}](\Delta t)^{-2} \, . \tag{29c}$$

So it is seen that the essential random errors are due in fact to the broadband noise such that $\tau_{c1,2} << \tau_{f,q} < \Delta t$. Also, because of the recurrent character of the algorithm the statistical retrieval error is accumulated with z so that its variance $D\varepsilon(z)$ is proportional to the number of recurrence cycles Q.

A rectangular-like pulse shape $f(\theta)$ with rise and decay time τ_r and duration τ is given by the expression

$$f(\vartheta) = \begin{cases} 0 & \text{for } \vartheta < 0 \\ \tau^{-1}[1 - \exp(-\vartheta / \tau_r)\,] & \text{for } \vartheta \in [0, \tau] \\ \tau^{-1}[1\text{-}\exp(-\tau / \tau_r)]\exp[-(\vartheta - \tau) / \tau_r] & \text{for } \vartheta \geq \tau \end{cases} \quad . \tag{30}$$

Such a shape has zero spectral components. Therefore, the Fourier deconvolution algorithm is not applicable in this case. The Volterra-deconvolution algorithm also leads to some problems. Nevertheless, the following recurrence deconvolution algorithm has been derived (Dreischuh et al., 1996; Gurdev et al., 1998):

$$P_s(z) = (c\tau / 2)[P_l^I(z) + (c\tau_r / 2)P_l^{II}(z)] + P_s(z - c\tau / 2) \ . \tag{31}$$

The deconvolution error $\delta(z)$ caused by the discrete data processing is obtained in the form

$$\delta(z) = -(1/30)\{(\Delta z)^4 P_s^{\mathrm{IV}}(z) + \sum_{i=0}^{Q}[2(c\tau / 2)(c\tau_r / 2)(\Delta z)^4]P_l^{\mathrm{VI}}(z - ic\tau / 2) \ . \tag{32}$$

In the case of broadband noise N with correlation times $\tau_{c1,2} < \tau_f, \tau_q$ ($\tau_f = \tau$), the random error variance $D\varepsilon$ is estimated to be

$$D\varepsilon(z) \sim (Q+1)[D_{N_1}(z)(\tau_{c1}/\tau_f)(1+\tau_r^2/\tau_f^2) + D_{N_2}(\tau_f^2\tau_{c2}/\tau_q^3)(1+\tau_r^2/\tau_q^2)]. \quad (33)$$

If in addition $\tau_{f,q} < \Delta t$, instead of the estimate (33) we obtain

$$D\varepsilon(z) \sim (Q+1)[D_{N_1}(z) + D_{N_2}][1+\tau_r^2/(\Delta t)^2]. \quad (34)$$

The simplest exponentially-shaped pulses have the following shape:

$$S(\vartheta) = \begin{cases} 0 & \text{for } \vartheta < 0 \\ (\vartheta/\tau^2)\exp(-\vartheta/\tau) & \text{for } \vartheta \geq 0 \end{cases}. \quad (35)$$

Although the Fourier and Volterra deconvolution algorithms are applicable in this case, we have obtained another simpler and faster algorithm (Gurdev et al., 1996), namely

$$P_s(z) = P_l(z) + c\tau P_l^I(z) + (c\tau/2)^2 P_l^{II}(z) \ . \quad (36)$$

The calculation error and the variance of the error due to the noise for $\tau_{c1,2} << \tau_{f,q}$ are evaluated as follows:

$$\delta(z) = -(c\tau/30)(\Delta z)^4[P_l^{V}(z) + (c\tau/2)P_l^{VI}(z)] \quad (37)$$

and

$$D\varepsilon(z) \sim (\tau_{c1}/\tau_f)(1+4\tau^2/\tau_f^2+\tau^4/\tau_f^4)D_{N_1}(z) + (\tau_{c2}/\tau_q)(1+4\tau^2/\tau_q^2+\tau^4/\tau_q^4)D_{N_2} \ . \quad (38)$$

For $\tau_{f,q} < \Delta t$, instead of (38) we have

$$D\varepsilon(z) \sim [D_{N_1}(z) + D_{N_2}][1+4\tau^2/(\Delta t)^2 + \tau^4/(\Delta t)^4] \ . \quad (39)$$

The restoration of the short-pulse lidar profile $P_s(z)$ allows one not only to improve the accuracy and the resolution of the lidar sensing but to develop methods as well for linear-strategy optical tomography of translucent scattering objects. For this purpose, one should measure, in combination with a lateral scan, the backscattering signal profile and the pulse energy passing through the object along each current line of sight at both the mutually opposite directions of sensing as it is shown in Fig.2.

In this way, the spatial distribution of the backscattering and extinction coefficients within the objects can be determined (Gurdev et al., 1998). Indeed, the forward illumination short-pulse lidar equation can be written in the form [see Eqs.(6) and (7)]

$$S(z) = S_1(z) = E_{01}\beta(z)\exp[-2\int_{z_1}^{z}\alpha_t(z')dz'] \ , \quad (40)$$

where E_{01} is the forward propagating sensing-pulse energy, $S(z)=S_1(z)=2P_{S1}(z)z^2/[cAK\eta(z)]$ is the so-called lidar S-function, $P_{S1}(z)$ is the lidar profile, and z_1 is the longitudinal coordinate (along the LOS) of the entrance of the sensing pulse/beam into the object. The final coordinate z_2 of the beam axis through the object is in fact the coordinate of the entrance into

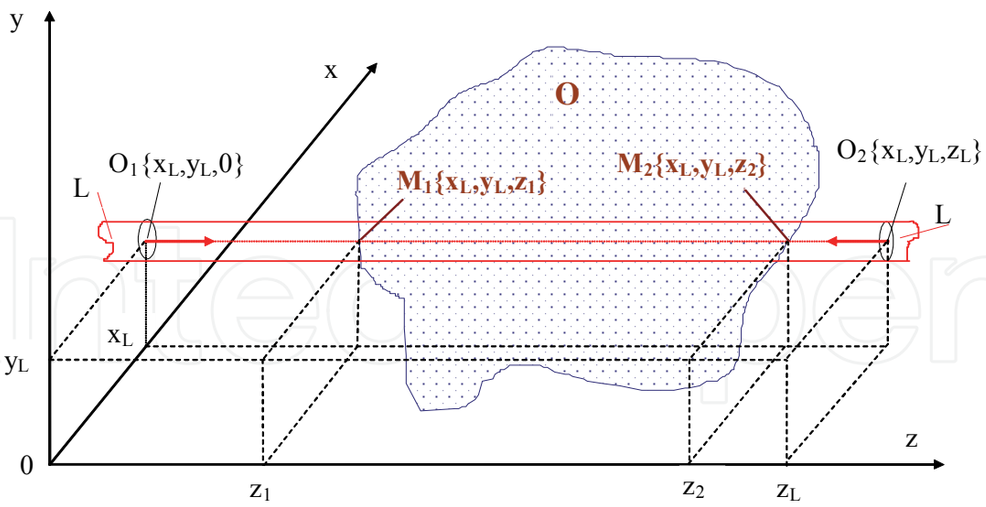

Fig. 2. Illustration of the backscattering and extinction coefficient reconstruction approach based on lidar principle. A right-handed rectangular coordinate system {0xyz} is used to determine uniquely the coordinates of the points within the investigated object O, the positions ($O_1\{x_L,y_L,0\}$ and $O_2\{x_L,y_L,z_L\}$) and orientations (**O_1O_2** and **O_2O_1**) of the lidar transceiver system L, the sensing-radiation path of propagation (the line of sight, $\overline{O_1O_2}$), and the coordinates $M_1\{x_L,y_L,z_1\}$ and $M_2\{x_L,y_L,z_2\}$ of the initial and the final scattering volumes, respectively, along the LOS. The object O is irradiated from two reciprocally opposite directions along each LOS chosen here to be parallel to axis 0z.

the object of the backward propagating (along **O_2O_1** direction) sensing pulse. The backward sensing *S*-function $S_2(z)=2P_{S2}(z_L-z)\,(z_L-z)^2/[cAK\eta(z_L-z)]$ is described by the equation

$$S_2(z) = E_{02}\beta(z)\exp[-2\int_z^{z_2}\alpha_t(z')dz'] \quad , \tag{41}$$

where E_{02} and $P_{S2}(z)$ are the corresponding sensing-pulse energy and lidar profile, and z_L is the new longitudinal coordinate of the transceiver lidar system (Fig.2). On the basis of Eqs.(40) and (41) it is not difficult to obtain that

$$\beta(z) = [S_1(z)S_2(z)/(E_{t1}E_{t2})]^{1/2} \quad , \tag{42}$$

and

$$\alpha_t(z) = 0.25\{\ln[S_2(z)/S_1(z)]\}' \quad , \tag{43}$$

where the corresponding lidar profiles $P_{S1}(z)$ and $P_{S2}(z)$ (in S_1 and S_2) and transmitted pulse energies $E_{t1} = E_{01}\exp[-\int_{z_1}^{z_2}\alpha_t(z)dz]$ and $E_{t2} = E_{02}\exp[-\int_{z_1}^{z_2}\alpha_t(z)dz]$ are to be measured experimentally; the prime in Eq.(43) denotes first derivative with respect to *z*.

The noise-induced random errors $\delta_\beta(z)$ and $\delta_\alpha(z)$ in the determination of $\beta(z)$ and $\alpha_t(z)$, respectively, are estimated (Gurdev et al., 1998) as follows:

$$\delta_\beta(z) = <[\beta_m(z)-\beta(z)]^2>^{1/2}/\beta(z) \sim \{0.25[\delta^2 P_{s1}(z)+\delta^2 P_{s2}(z)]+\delta_E^2\}^{1/2} \tag{44}$$

and

$$\delta_\alpha(z) = \left\langle [\alpha_{tm}(z) - \alpha_t(z)]^2 \right\rangle^{1/2} \quad < \quad 0.25[(D\varepsilon)^{1/2} / \rho][P_{s1}^{-2}(z) + P_{s2}^{-2}(z)]^{1/2}\{1 + \rho[r_1^{-2}(z) + r_2^{-2}(z)]\}^{1/2}, \quad (45)$$

where $\beta_m(z)$ and $\alpha_{tm}(z)$ are the backscattering and extinction profiles, respectively, calculated on the basis of the experimental data, $\beta(z)$ and $\alpha_t(z)$ are the corresponding true profiles, $\delta^2 P_{s1,2}(z) = D\varepsilon_{1,2}(z)/P^2_{s1,2}(z)$ are the relative variances of the random errors ε_1 and ε_2 in the determination of P_{s1} and P_{s2}, $\delta_E^2 = \langle (E_{tm}-E_t)^2 \rangle / E_t^2$ is the relative variance of the transmitted pulse energy with measured value E_{tm} and true value E_t, $D\varepsilon(z)=\max\{D\varepsilon_{1,2}(z)\}$, ρ is an estimate of the correlation radius of the random functions $\varepsilon_{1,2}(z)$, and $r_{1,2}(z)=|P_{s1,2}(z)/P'_{s1,2}(z)|$. When ρ is smaller than the computing step Δz, one should replace it by Δz in Eq.(45). According to Eqs.(44) and (45), the higher the signal-to-noise ratio (the smaller $\delta P_{s1,2}$ and δ_E) the smaller the random errors δ_β and δ_α. In addition, δ_α depends on the spectral properties of the noise (ρ) in combination with the signal variability ($r_{1,2}$).

The efficiency of the deconvolution techniques discussed in this section and their performance are tested and confirmed by detailed computer simulations. Some of the models employed and results obtained are illustrated in Figs.3-5. The sampling interval Δt_0 is assumed to be equal to 0.1 μs corresponding to Δz_0= 15m. Models of a maximum-resolved lidar profile $P_s(z)$ and the corresponding detected lidar return $P_l(z)$ [see Eq.(10)] in the case of pulse response function $f(\theta)$ given in the inset are shown in Fig.3. As can be seen, $P_s(z)$ consists of some mean profile, a high-resolution component in the near field, and a double-peak structure introducing discontinuities at a further range. The system response function $f(\theta)$ is chosen to have a shape close to this of the typical TEA-CO_2 laser pulses. It consists of an initial spike followed by a long tail. As a result of the effect of convolution, important information about the small-scale variations of the backscattering within the long-resolution cell (about 200-300 m) is lost in the registered long-pulse profile $P_l(z)$. In the absence of noise the deconvolution procedures ensure accurate retrieval of the short-pulse profile $P_s(z)$. Then the restored profiles $P_{sc}(z)$ do not differ visibly from the original model $P_s(z)$. As it is shown in Gurdev et al., 1993, the systematic errors due to discrete data processing can be of the order of or smaller than 1% on the average. The random noise influence on the retrieval accuracy is simulated assuming that $\tau_{c1,2} << \tau_{f,q}$, $\tau_q << \tau_f$ and even $\tau_q < \Delta t_0$ as it is in the atmospheric lidars. In this case, at comparable noise levels N_1 and N_2 , the influence of the stationary background component N_2 will be dominating [see Eqs.(11), (17), (24a), (29a), (33), and (38)]. Therefore, we have simulated a stationary effective additive noise n corresponding to the convolution of N_2 and the receiving system response q. The correlation time τ_c of the noise n is of the order of τ_q and may be both larger and smaller than Δt_0. In the latter case we have in practice a white noise with restricted frequency band ($\omega < \pi/\Delta t_0$) due to sampling. The effective correlation time of such a noise is equal to Δt_0. In the simulations we have generated white noise ($\tau_c \sim \Delta t_0$) and Gaussian-correlation noise ($\tau_c > \Delta t_0$). The noise level is specified by the (signal-to-noise, SNR) ratio of the minimum of the double-peak structure of $P_s(z)$ (see Fig.3) to the standard deviation of the noise n.

In Fig.4, the original short-pulse profile $P_s(z)$ is compared with the profiles $P_{sr}(z)$ restored by using Fourier deconvolution in the presence of white noise with SNR=50. As seen in Fig.4a, the deconvolution leads to an increase of the noise influence and the error magnitude considerably exceeds the oscillation amplitude of the retrieved profile. So, some type of controllable low-pass filtering is necessary, retaining at the same time an improved retrieval resolution. In

Fig.4b such a filtering is realized by increasing the computing step up to $\Delta t=4\Delta t_0$. The results from filtering the measured lidar profiles $P_{lm}(z)$ by a smooth monotonic low-pass filter with $4\Delta t_0$-wide window are shown in Fig.4c. As seen, both types of processing lead to similar restored profiles with considerable reduction of the noise effect [see Eq.(19)].

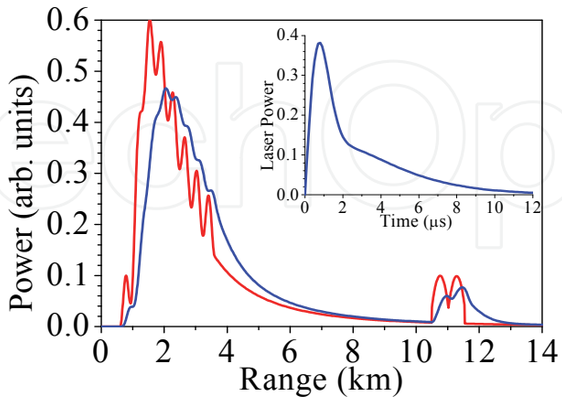

Fig. 3. Short-pulse lidar profile $P_s(z)$ (red) and the corresponding detected lidar return $P_l(z)$ (blue) obtained for the pulse response shape $f(\theta)$ (inset).

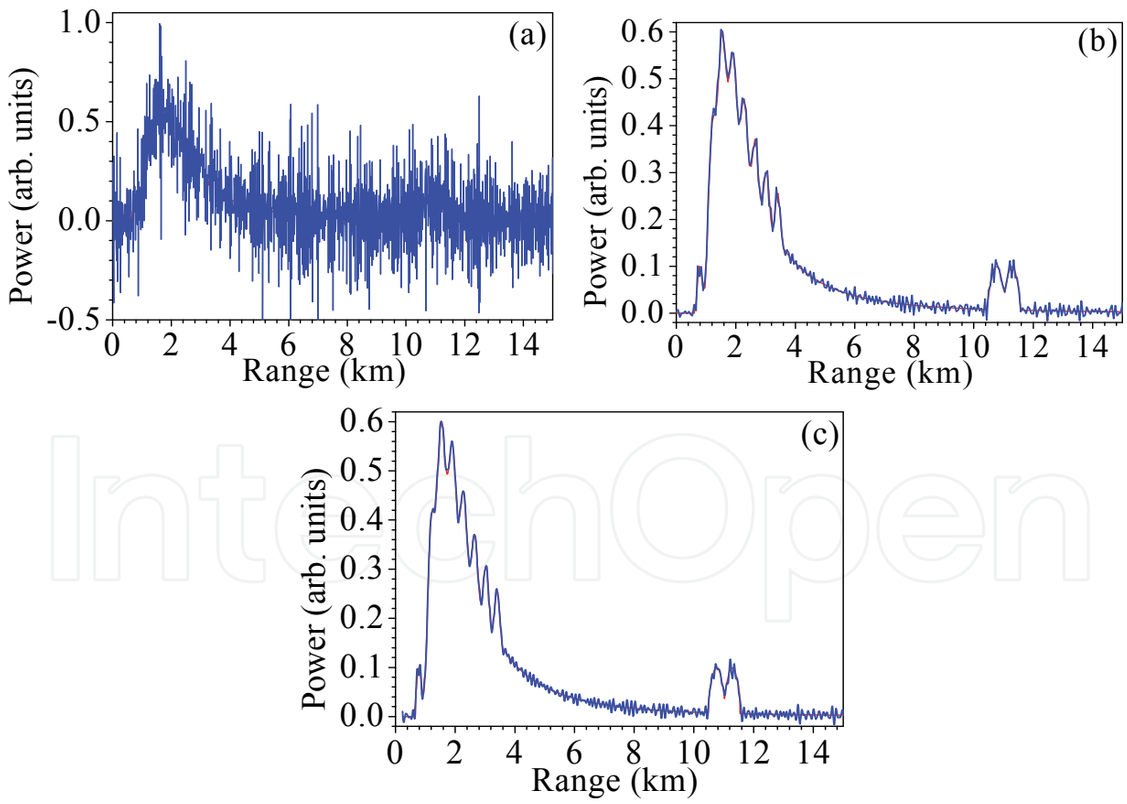

Fig. 4. Profile $P_s(z)$ (red) and the profile restored by use of Fourier deconvolution (blue), in the presence of white Gaussian-distributed noise with SNR=50, at $\Delta t=\Delta t_0$ (a), $\Delta t=4\Delta t_0$ (b), and when using a smooth monotonic filter with a $4\Delta t_0$-wide window applied to the measured lidar profile (c).

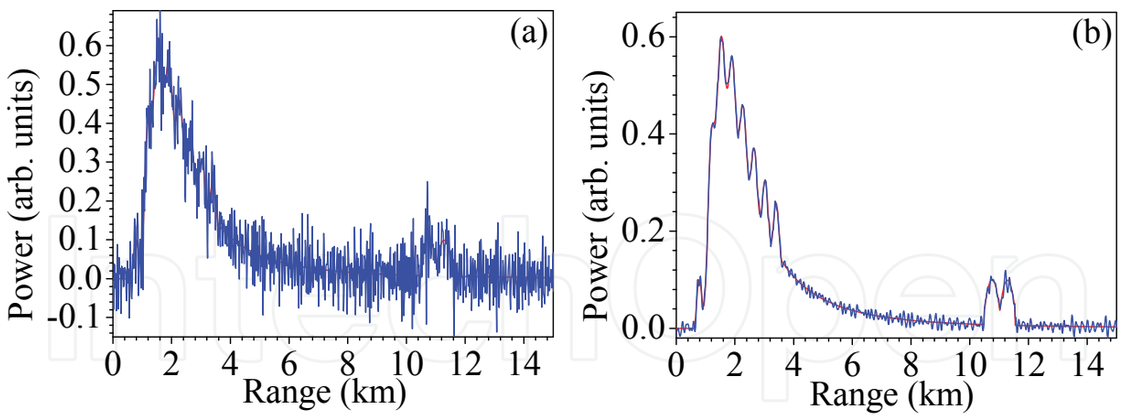

Fig. 5. Profile $P_s(z)$ (red) and the profile restored by use of Fourier deconvolution (blue) in the presence of additive Gaussian correlated and distributed noise with SNR=50 and correlation time $\tau_c=2\Delta t_0$ (a) and $5\Delta t_0$ (b).

The effect of the correlated noise with $\tau_c>\Delta t_0$ (i.e., $\tau_c\sim\tau_q>\Delta t_0$) is gradually lower than that of the white noise [see Eq.(19)]. It is illustrated in Fig.5 where the profiles $P_{sr}(z)$ are shown restored by Fourier deconvolution in the presence of correlated Gaussian noise with $\tau_c=2\Delta t_0$ and $5\Delta t_0$ and SNR=50. As expected, the error magnitude decreases with increasing the correlation time of the noise and at $\tau_c=5\Delta t_0$ the accuracy of the deconvolved lidar profiles is satisfactory even without any filtering applied.

The efficiency of the Fourier deconvolution approach is demonstrated as well in Stoyanov et al., 1996, where data (backscattering power profiles) have been processed, obtained by the National Oceanic and Atmospheric Administration (NOAA) pulsed coherent CO_2 Doppler lidar.

In Fig.6, the profile $P_l(z)$ is shown obtained by convolution of $P_s(z)$ with a rectangular-like sensing laser pulse with $\tau=2$ μs and $\tau_r=0.1$ μs. The recovered by algorithm (31) profiles $P_{sr}(z)$ in the presence of white noise at SNR=50 are represented in Fig.7. As it is seen, the noise influence is strong if no filtering is employed (Fig.7a). At the same time, increasing the computing step [Eq.(34)] up to $\Delta t=4\Delta t_0$ (Fig.7b) or filtering $P_{lm}(z)$ using a smooth monotonic low-pass filter with $4\Delta t_0$-wide window (Fig.7c) lead to comparable substantial reduction of the noise effect at minimum distortion of $P_{sr}(z)$ with respect to $P_s(z)$. The intrinsic noise

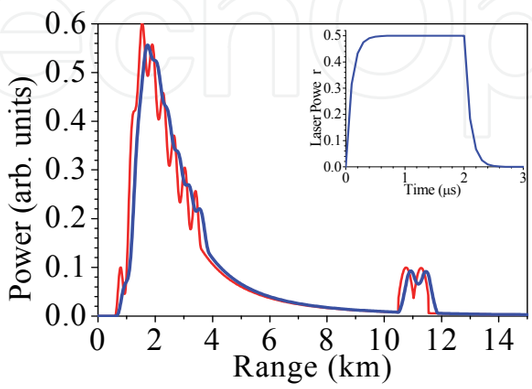

Fig. 6. Short-pulse lidar profile $P_s(z)$ (red) and the corresponding detected lidar return $P_l(z)$ (blue) obtained for the rectangular-like pulse response shape $f(\theta)$ given in the inset.

accumulation with the range is also noticeable. In Fig.8 it is shown that the effect of a correlated noise (with $\tau_c \sim \tau_q > \Delta t_0$) on the retrieval accuracy is considerably lower compared to the effect of white noise. In agreement with the theoretical results [Eq.(33)], the retrieval error decreases with increasing the correlation time of the noise. At $\tau_c = 5\Delta t_0$ the accuracy of the restored profiles is quite acceptable without any filtering performed.

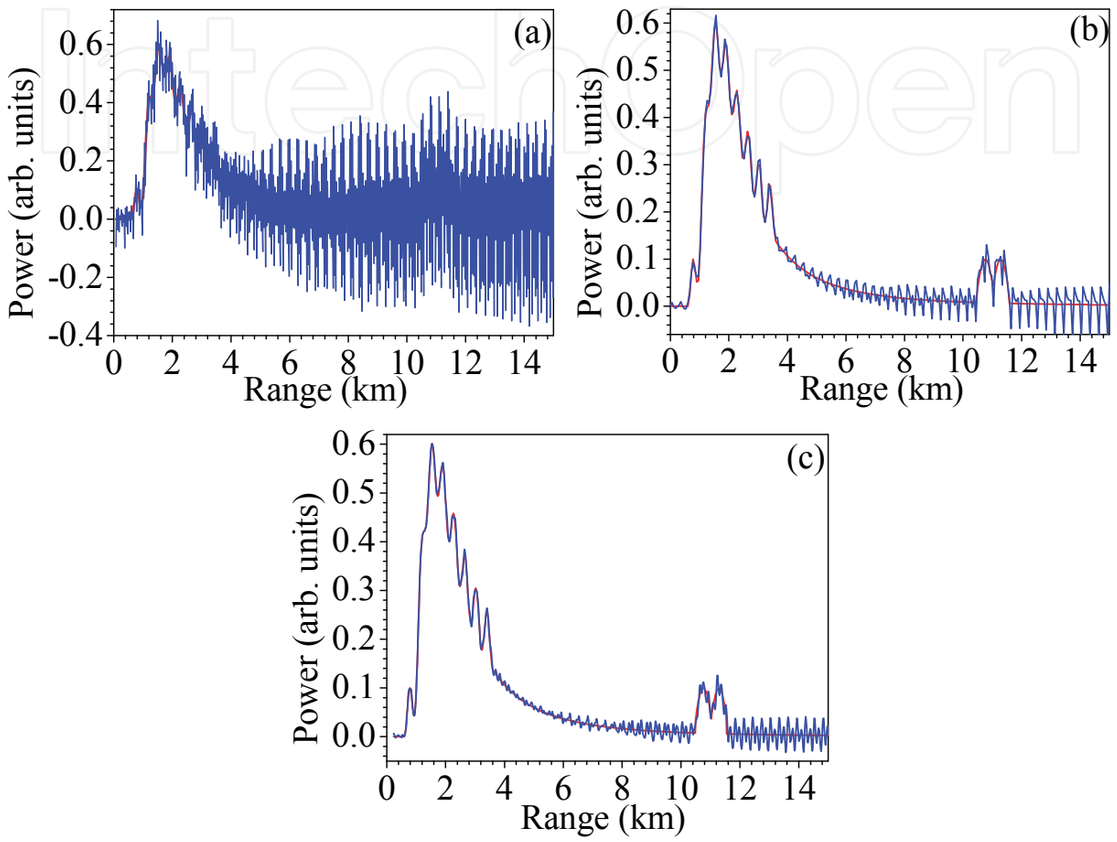

Fig. 7. Profile $P_s(z)$ (red) and the profile restored by use of Fourier deconvolution (blue), in the presence of white Gaussian-distributed noise with SNR=50, at $\Delta t = \Delta t_0$ (a), $\Delta t = 4\Delta t_0$ (b), and when using a smooth monotonic filter with a $4\Delta t_0$-wide window applied to the measured lidar profile (c).

The investigations described in this section show that deconvolution techniques can be successfully used for improving the accuracy and resolution of sensing the atmosphere or other objects by long-pulse elastic direct-detection lidars. At negligibly weak noise a high accuracy in the restoration of the short-pulse lidar profile is achievable at short-enough computing step. Also, the uncertainties in the lidar pulse response function lead to some characteristic retrieval distortions that can be reduced to some extent by using suitable approaches. Even at high initial SNR, a broadband noise, i.e., fast fluctuations with correlation time below the sensing-pulse duration, can cause considerable noise effect such that the retrieved short-pulse lidar profile is fully disguised. In this case, the noise influence can be effectively reduced by using appropriate filtering or choice of the computing step. The filter window or the computing step should exceed the fluctuation correlation time. At

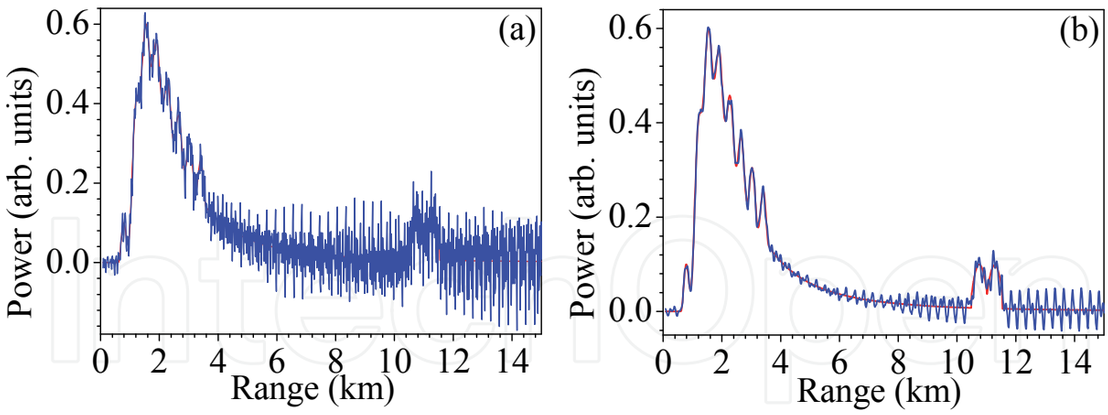

Fig. 8. Profile $P_s(z)$ (red) and the profile restored by use of Fourier deconvolution (blue) in the presence of additive Gaussian correlated and distributed noise with SNR=50 and correlation time $\tau_c=2\Delta t_0$ (a) and $5\Delta t_0$ (b).

the same time, they should be smaller than the least variation scale of the short-pulse lidar profile to avoid essential distortions and lowering of the retrieval resolution. Note as well that the deconvolution algorithm performance decreases the effect of narrow-band noise whose correlation time substantially exceeds the pulse duration. At last, let us mention one more virtue of the deconvolution-based retrieval of the short-pulse lidar profiles. That is, it allows high-resolution sensing of small finite-size objects by longer laser pulses, realizing in this way double-sided linear-strategy optical tomography of such objects.

4. Deconvolution-based improvement of the accuracy of measuring electron temperature profiles in tokamak plasmas by Thomson scattering lidar

The electron temperature T_e and density n_e distributions in the torus are basic characteristics of the tokamak fusion plasma. They are conditioned by the modes of heating and confinement of the high-temperature plasma as well as by the different oscillatory movements of the plasma particles sometimes leading to the appearance of crucial instabilities. Thus, the T_e and n_e profiles are not only important factors of the development and the efficiency of the fusion process but indicators as well of the dynamic plasma state. So far, the most appropriate approach to their simultaneous express determination in a remote contactless way is the Thomson scattering (TS) lidar approach (Salzmann et al., 1988; Kempenaars et al., 2008, 2010). It allows one to obtain the T_e and n_e profiles along a LOS through the torus core. The minimum range resolution interval achievable by the contemporary core TS lidars (Kempenaars et al., 2010) is about 12-15 cm. Such a resolution is relatively good in general, but is insufficient for resolving small-scale inhomogeneities and the edge pedestal areas of T_e and n_e profiles in the so-called high-confinement mode (H-mode) of operation of the tokamak reactors. A way of improving the range resolution of the TS lidars is based on the use of deconvolution techniques for recovering the high-resolution lidar profiles. The deconvolution procedures, however, increase the influence of the noise. Therefore, to achieve acceptable recovered profiles one should apply a final filtering that lowers the sensing resolution to some compromise extent. The statistical modeling is a way to outline some optimal conditions under which the deconvolution techniques lead to satisfactory high-resolution restoration of the T_e profiles (Stoyanov et al., 2009; Dreischuh et al., 2011).

The TS lidar return signal from fussion plasma as well as the plasma light background and other additive noise are convenient to be analyzed on the basis of an equivalent photon counting procedure (Gurdev et al., 2008b). Based on Eqs.(1), (4) and (9), the long-pulse lidar equation in this case, for some say m-th spectral interval $[\lambda_{s1m}, \lambda_{s2m}]$, is expressible as

$$N_l(\lambda_{s1m}, \lambda_{s2m}; z) = N_{lm}(z) = (2/c)\int_0^z dz' f[2(z-z')/c] N_s(\lambda_{s1m}, \lambda_{s2m}; z), \tag{46}$$

where the maximum-resolved lidar profile N_s is described by the short-pulse lidar equation

$$N_s(\lambda_{s1m}, \lambda_{s2m}; z) = N_{sm}(z) = (c/2) A N_0(\lambda_i) \int_{\lambda_{s1m}}^{\lambda_{s2m}} d\lambda_s K(\lambda_i, \lambda_s) \Phi(\lambda_i, \lambda_s; z); \tag{47}$$

$K(\lambda_i,\lambda_s)=K_t(\lambda_i)K_t(\lambda_s)K_f(\lambda_s)EQE(\lambda_s)$; $K_t(\lambda_i)$, $K_t(\lambda_s)$, $K_f(\lambda_s)$ and $EQE(\lambda_s)$ are respectively the wavelength-dependent optical transmittance of the plasma-irradiating path, the optical transmittance of the scattered-light collecting path, the receiver filter spectral characteristic, and the effective quantum efficiency of the photon detection accounting for the quantum yield and the Poisson fluctuations of the photoelectron number after the photocathode enhanced in the process of cascade multiplying in the employed microchannel tube; $\Phi(\lambda_i, \lambda_s; z)$ is given by Eq.(2) with $T(\lambda_i,\lambda_s;z) \equiv 1$, $\beta(\lambda_i;z)=\beta(z)=n_e(z)r_0^2$, and

$$\begin{aligned} L[\lambda_s, \lambda_i; z] = {} & \frac{c}{\sqrt{\pi}\lambda_i v_{th}(z)} \left(1 + \frac{15}{16}\frac{v_{th}^2(z)}{c^2} + \frac{105}{512}\frac{v_{th}^4(z)}{c^4}\right)^{-1} \frac{(\lambda_i/\lambda_s)^3}{(1+\lambda_i/\lambda_s)}; \\ \times \quad & \exp\left\{-\frac{c^2}{v_{th}^2(z)}\left[(\lambda_i/\lambda_s)^{1/2} + (\lambda_s/\lambda_i)^{1/2} - 2\right]\right\} q[\lambda_i, \lambda_s, T_e(z)] \end{aligned} \tag{48}$$

$r_0=e^2/(4\pi\varepsilon_0 m_e c^2)$ is the classical electron radius, e and m_e are respectively the electron charge and rest mass, ε_0 is the dielectric constant of vacuum, $v_{th}(z)=[2k_B T_e(z)/m_e]^{1/2}$ is the rms thermal velocity of the electrons, k_B is the Boltzmann constant, $n_e(z)$ and $T_e(z)$ are respectively the electron density and temperature profiles along the lidar LOS, and $q[\lambda_i,\lambda_s,T_e(z)]$ is the depolarization term accounting for the relativistic depolarization effects on the backscattered radiation. For scattering at 180° the depolarization can be expressed in terms of exponential integral $E_n(p)$ (Naito et al., 1993):

$$q[\lambda_i, \lambda_s, T_e(z)] = 1 + 2e^p\left[E_3(p) - 3E_5(p)\right] = 1 + \frac{1}{2}\left\{\frac{p^3}{2} - \frac{p^2}{2} - p - 1\right\} + p^2\left(1 - \frac{p^2}{4}\right)e^p E_1(p) \tag{49}$$

$$p = \frac{m_e c^2}{2k_B T_e(z)}\left(\sqrt{\lambda_s/\lambda_i} + \sqrt{\lambda_i/\lambda_s}\right), \text{ and } \quad E_n(p) = \int_1^\infty \frac{e^{-px}}{x^n} dx .$$

The TS lidar signal is accompanied by the plasma light background that is a serious source of error in the determination of T_e. Its emissivity spectrum per unit solid angle, mainly due to the bremsstrahlung, is given by the expression (Sheffield, 1975; Foord et al., 1982) :

$$\frac{dE}{d\Omega} = \frac{0.95\times10^{-19}}{\lambda\ 4\pi} n_e^{\ 2}(z) Z_{\text{eff}}(z)[k_B T_e(z)]^{-1/2} \exp\left(-\frac{hc}{\lambda k_B T_e(z)}\right)\tilde{g}_{ff}(\lambda, T_e), \tag{50}$$

where Z_{eff} (z) is the effective ion charge, the quantities $k_{\mathrm{B}}T_{\mathrm{e}}$ and hc/λ are in eV, $\exp[-hc/(\lambda k_{\mathrm{B}}T_{\mathrm{e}})]\approx 1$ and $\tilde{g}_{ff}(\lambda, T_e)$ is the so-called Gaunt factor that depends weakly on T_{e} and on the radiation wavelength λ, and accounts for the quantum effects, the electron screening of nuclei, etc. (Brusaard & van de Hulst, 1962). For the photoelectron rate characterizing the parasitic background due to plasma light penetrating into the m-th spectral channel we obtain the following expression:

$$N_{\mathrm{bm}}(\lambda_{\mathrm{s}1m}, \lambda_{\mathrm{s}2m}) = 6.25\times 10^{-21} A_D \Delta\Omega_D \times \int_z dz n_{\mathrm{e}}^2(z)\left[k_{\mathrm{B}}T_{\mathrm{e}}(z)\right]^{-1/2} \int_{\lambda_{\mathrm{s}1m}}^{\lambda_{\mathrm{s}2m}} d\lambda_{\mathrm{s}} K_t(\lambda_{\mathrm{s}}) K_f(\lambda_{\mathrm{s}}) EQE(\lambda_{\mathrm{s}}) \lambda_{\mathrm{s}}^{-1} \ln\left[k_{\mathrm{B}}T_{\mathrm{e}}(z)/(13.6h^2c^2/\lambda_{\mathrm{s}}^2)^{1/3}\right], \quad (51)$$

where A_D is the photon detector effective area and $\Delta\Omega_D$ is the solid angle determined by the relative aperture of the receiving optics. In order to take into account additional background light sources, an enhancement factor is included in the simulations.

The center-of-mass wavelength (CMW) approach (Gurdev et al., 2008b; Dreischuh et al., 2009) to the determination of the electron temperature profiles $T_{\mathrm{e}}(z)$ in fusion plasma is based on the unambiguous temperature dependence of the CMW of the relativistic Thomson backscattering spectrum. The TS lidar profiles N_{sm} are measured for M selected spectral intervals $[\lambda_{\mathrm{s}1\mathrm{m}}, \lambda_{\mathrm{s}2\mathrm{m}}]$ (m=1,2,…,M) [see Eq.(48)]. The CMW λ_{CM} defined as

$$\lambda_{\mathrm{CM}}(T_{\mathrm{e}}; z) = \left(\sum_m \lambda_m N_{sm}(z)\right) / \left(\sum_m N_{sm}(z)\right) \quad (52)$$

is unambiguous function of the electron temperature (see also Fig.10 below); $\lambda_m=(\lambda_{s1m}+\lambda_{s2m})/2$ is the central wavelength of the m-th interval. Then the temperature is determined on the basis of the inverse function $T_{\mathrm{e}}(\lambda_{\mathrm{CM}}, z)$.

The linear error propagation approach leads to the following expression of the rms error δT_{e} in the determination of T_{e} on the basis of the dependence $\lambda_{\mathrm{CM}}= f(T_{\mathrm{e}})$ (Gurdev et al., 2008b):

$$\delta T_{\mathrm{e}} = \left|d\ln\lambda_{\mathrm{CM}}(T_{\mathrm{e}})/dT_{\mathrm{e}}\right|^{-1}\left(\sum_m N_{pm}\tau_q\right)^{-1}\left\{\sum_{m=1}^{M}\left(\frac{\lambda_m-\lambda_{\mathrm{CM}}}{\lambda_{\mathrm{CM}}}\right)^2 N_{pm}\tau_q(1+N_{\mathrm{b}m}/N_{pm})\right\}^{1/2}, \quad (53)$$

where N_{pm} is the convolution of the laser pulse shape and the short-pulse lidar profile. The determinant temporal factor in Eq.(53) is τ_q because it is in practice the signal integration time interval. In case of applying deconvolution techniques for recovering the short-pulse lidar profiles and thus for obtaining more accurate T_{e} profiles, instead of Eq.(53) we have (Dreischuh et al., 2011)

$$\delta T_{\mathrm{e}} = \left|d\ln\lambda_{\mathrm{CM}}(T_{\mathrm{e}})/dT_{\mathrm{e}}\right|^{-1}\left(\sum_m N_{sm}\tau_\varphi\right)^{-1}\left\{\sum_{m=1}^{M}\left(\frac{\lambda_m-\lambda_{\mathrm{CM}}}{\lambda_{\mathrm{CM}}}\right)^2 N_{sm}\tau_\varphi[1+\chi(\tau_{\mathrm{s}}/\tau_\varphi)N_{\mathrm{b}m}/N_{sm}]\right\}^{1/2}, \quad (54)$$

where τ_φ is the time-domain filter window and the factor $\chi(\tau_s/\tau_\varphi)$ is an increasing function of the ratio τ_s/τ_φ. This factor is accounting for the fact that the background is initially

smoothed (integrated) only by the receiving system response function while the deconvolution is performed using the total lidar response function including the laser pulse shape.
An estimate of the SNR for the m-th spectral channel could be written as follows:

$$SNR_m = \{N_{pm}\tau_q / (1 + N_{bm} / N_{pm})\}^{1/2} \tag{55}$$

in the case of convolved lidar profiles, and

$$SNR_m = \{N_{sm}\tau_\varphi / (1 + \chi(\tau_s / \tau_\varphi)N_{bm} / N_{sm})\}^{1/2} \tag{56}$$

in the case of deconvolved lidar profiles.
From Eqs.(53-56) evidently follows that the signal-to-noise ratios SNR_m are the main factor conditioning the statistical retrieval accuracy.
The characteristic parameters of the plasma and the TS lidar used in the simulations are chosen to be close to those of the core TS lidar system on the Joint European Torus (JET) (Casci et al., 2002; Salzmann et al., 1988; Kempenaars et al., 2008, 2010). The sensing laser radiation is assumed to have wavelength λ_i =694 nm and pulse energy $E_0=N_0hc/\lambda_i$ =1 J, and to be injected horizontally along the plasma midplane. The minor radius r of the torus, along the LOS, is supposed to be 1 m. Correspondingly, the plasma is supposed to occupy the region between R=2 m and R=4 m, R being the radial distance from the center of the torus (Casci et al., 2002). Assuming that the LOS coordinate of the center of the torus is z_c, we obtain that $R=z_c- z$. The number of receiving spectrometer channels is chosen to be six. Their absolute spectral responses, including the EQE of the detectors, are also close to those of JET TS core lidar (Kempenaars et al., 2010). In particular, the detectors considered in the simulations are multialkali microchannel plate photomultiplier tubes (MCP-PMTs) with response times of about 650 ps and EQE equal to 0.005 for channel 1 and 0.02 for the other five channels. TS spectrum is observed within the wavelength region from 350 nm to 850 nm. To correct the collection efficiency the values of the solid angle of acceptance given in Kempenaars et al., 2010 are used. They vary from 0.005 sr, at R=2 m, to 0.007 sr at R=4 m. The irradiating and collecting paths optical transmittances assumed are $K_t(\lambda_i)$=0.75 and $K_t(\lambda_s)$=0.25, respectively. The detector's etendue $E=A_D\Delta\Omega_D$ needed for the estimation of the plasma bremsstrahlung photoelectron rate is assumed to have a value of ~0.32 cm²sr. The factor of reducing the plasma bremsstrahlung conditioned by the plasma torus observation pupil is supposed to be 0.3. The effective atomic number of an equivalent plasma ion is chosen to be Z_{eff}=2. The bremsstrahlung background is added multiplied by an enhancement factor of 2 in order to take into account additional background light sources. The temporal sampling interval Δt_0 is supposed to be 200 ps (Δz_0=3 cm spatial interval).
The models of the temperature and density profiles used in the simulations consist of a smooth parabolic component whose parameters are chosen to simulate the real plasma conditions (Dreischuh et al., 2011; see also Figs. 12-14). Additionally, the $T_e(z)$ profile has a multiscale high-resolution component superimposed on the smooth component in order to illustrate the improvement of the retrieval accuracy and resolution depending on the noise level. The central electron density is varied in the range n_e= 2 ÷ 9 x10^{19} m^{-3} to simulate different plasma conditions and SNRs.
The sensing laser pulse shape is chosen to be $s(\theta) = (\theta/\tau_l^2)\exp(-\theta/\tau_l)$ for $\theta \geq 0$ and $s(\theta) = 0$ for $\theta < 0$, where τ_l is a time constant. Such a pulse shape can be a good approximation of various

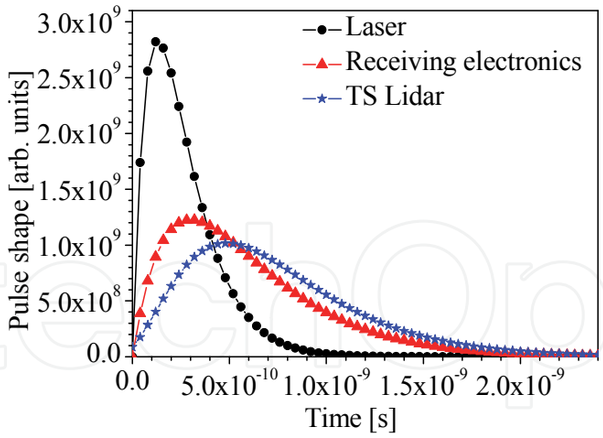

Fig. 9. Models of the laser pulse shape (circles), receiving system response shape (triangles) and the resulting TS lidar system response shape (stars) used in the simulations.

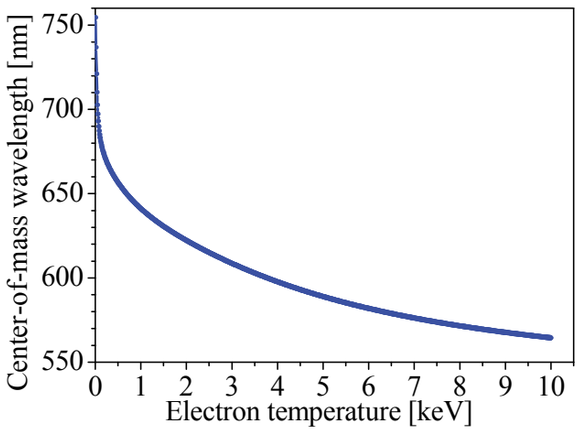

Fig. 10. Reference function $\lambda_{CM}(T_e)$ underlying the CMW approach.

real asymmetric laser pulses (e.g., Dong et al., 2001; Kondoh et al., 2001). The same model is used for the shape of the receiving system response function $q(\theta)$, that is, $q(\theta) = (\theta/\tau_e^2)\exp(-\theta/\tau_e)$ for $\theta \geq 0$, and $q(\theta) = 0$ for $\theta < 0$, where τ_e is another time constant. The Fourier spectrum modulus of the above pulse shapes is equal to $(1+\omega^2\tau_{l,e}^2)^{-1}$, i.e., it has no zeros, which is favorable for applying Fourier-deconvolution algorithm. The values of τ_l and τ_e are chosen so that the effective durations $\tau_s = e\,\tau_l$ and $\tau_q = e\,\tau_e$ of $s(\theta)$ and $q(\theta)$ to be respectively about 350 ps (τ_l = 130 ps) and 810 ps (τ_e= 300 ps). Then the effective duration of the resulting system response shape τ_f will be about 1 ns, which corresponds to 15 cm range resolution cell of the TS lidar. The models of the laser pulse shape, the receiving system response shape and the TS lidar system response shape are shown in Fig.9.

The reference function $\lambda_{CM}(T_e)$ is determined on the basis of the temperature dependence of the TS spectrum and is presented in Fig.10 for temperatures up to 10 keV. In the case of long-pulse sensing, when the pulse length exceeds the spatial scale of the temperature inhomogeneities, the temperature information provided by the lidar profiles from the different spectral channels will be distorted. Correspondingly, the recovered temperature

profiles will also be distorted with respect to the true ones. The role of the deconvolution here is to reduce, as much as possible at the corresponding noise level, the convolution-due distortions of the recovered T_e profiles.

The Monte-Carlo simulations are performed in the following way. First, the mean values $N_{sm}(z)$ of the TS signal in each spectral channel are determined and then convolved with the laser pulse shape in order to account for the real pulse duration. Next, the mean background photoelectron count rate $N_{bm}(z)$ is evaluated. Then, assuming Poisson statistics of the signal and background photoelectrons within a Δt_0 - long interval and using random – number generator, J realizations of the TS signal $N_{lm}(z)\Delta t_0$ and background $N_{bm}(z)\Delta t_0$ photoelectrons are produced (see Fig11). Further, the receiving system response function is taken into account performing the convolution with it of the profiles of the background and signal count rates in each channel. Assuming an accurate measurement of the mean convolved background count rate, it is subtracted from the corresponding background count rate realizations. Thus, the convolved background count rate fluctuations are obtained. At last, the obtained realizations of the long-pulse lidar profiles including the background fluctuations are deconvolved using the system response function $f(\theta)$. The center of mass wavelength as a function of the coordinate along the LOS is determined according to Eq.(52) on the basis of the deconvolved profiles, and is used together with the reference function $\lambda_{CM}(T_e)$ for obtaining J estimates $\hat{T}_{ej}(z)$ of the electron temperature profile $T_e(z)$, j=1,2,…,J. Then, an estimate $\delta\hat{T}_e(z)$ of the measurement error is obtainable as

$$\delta\hat{T}_e(z) = \left\{ J^{-1} \sum_{j=1}^{J} [\hat{T}_{ej}(z) - T_e(z)]^2 \right\}^{1/2}.$$

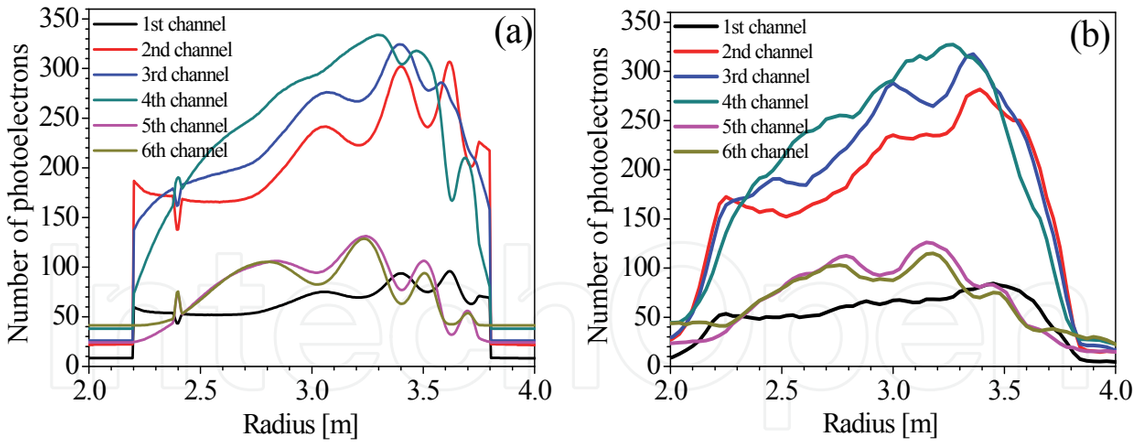

Fig. 11. TS lidar profiles: (a) mean short-pulse lidar profiles including the mean plasma light background, (b) realizations of the measured long-pulse lidar profiles including the background realizations; n_e = 9x10^{19} m^{-3} .

To simulate correctly the detection of the analog signals, the convolved profiles are calculated almost ideally by a computing step much less than Δt_0. The real ADC step Δt_0 is used when processing further the long-pulse profiles. The obtained mean short-pulse lidar profiles and simulated realizations of the measured long-pulse lidar profiles for the six spectral channels are shown in Figs.11a,b.

As an illustration of the deconvolution effect, the T_e profiles restored in the absence of noise on the basis of the convolved and deconvolved lidar profiles are shown in Fig.12. As it is seen, the direct use of the long-pulse lidar profiles leads to significant distortions in the restored electron temperature profiles. After applying deconvolution techniques to the long-pulse lidar profiles, at negligible noise level the T_e profiles are determined with considerably higher accuracy, and resolution scale of the order of the sampling interval Δz_0.

Because of the strong Poisson fluctuations, some type of low-pass noise filtering is necessary to ensure a satisfactory quality of the restored profiles. However, the filtering procedure lowers the range resolution. The range resolution cell will be already of the order of the width W of the range-domain window of the filter employed. To retain a satisfactory range resolution the value of W should be less than the least variation scale (along the line of sight) of the temperature profile. Then the restored temperature profiles are minimally distorted with respect to the true ones. Different low-pass digital filters are used in the numerical simulations. Results presented below are obtained using filers with $2\Delta z_0$ and $3\Delta z_0$ –wide windows for smoothing the recorded lidar profiles.

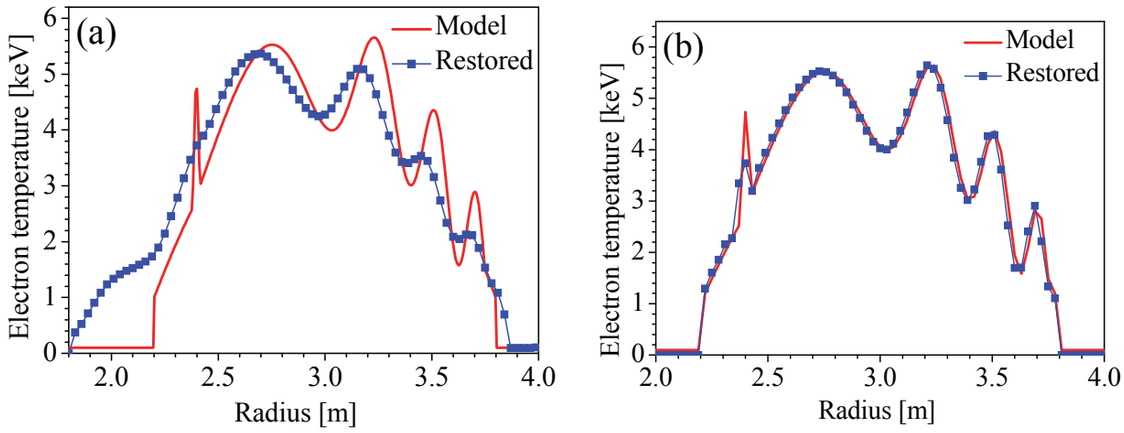

Fig. 12. Electron temperature profiles restored in absence of noise on the basis of the convolved (a) and deconvolved (b) lidar profiles; $n_e = 9\text{x}10^{19}$ m^{-3}.

In Fig.13 the profiles of the electron temperature restored on the basis of the measured convolved and deconvolved lidar profiles for one realization of the Poisson noise are presented. It is well seen that the temperature profiles restored on the basis of convolved lidar profiles (Fig.13a) are essentially distorted with respect to the original model. At the same time, the temperature profile restored on the basis of deconvolved lidar profiles (Fig.13b) is disguised by strongly increased fluctuations. In order to suppress the deconvolution-due increase of the noise, noise controlling filters have been applied (Figs.13c,d) ensuring acceptable accuracy and resolution of the restored electron temperature profiles. It is seen in Fig.13d that even $2\Delta z_0$–wide filter window (corresponding to 6 cm range resolution) ensures good quality of the obtained T_e profile. The theoretical statistical errors presented in these figures are estimated assuming empirically in Eq.(54) that $\chi(\tau_s/\tau_\varphi) = 25$ (Fig.13b), 15 (Fig.13c), and 10 (Fig.13d). When using convolved profiles for determination of T_e (Fig.13a), the factor $\chi(\tau_s/\tau_\varphi)$ is not of importance [Eq.(53)]. In this

case, the "empirical" statistical error is estimated by simulations with respect to the temperature profile obtained from the convolved, long-pulse lidar profiles in absence of noise. The same as the above-described is the behavior of the restored profiles in the case of lower electron concentration n_e = 2x10^{19} m^{-3}. Because of the lower SNR in this case, the quality of the restored profiles is somewhat lower compared to the case of n_e=9x10^{19} m^{-3}.

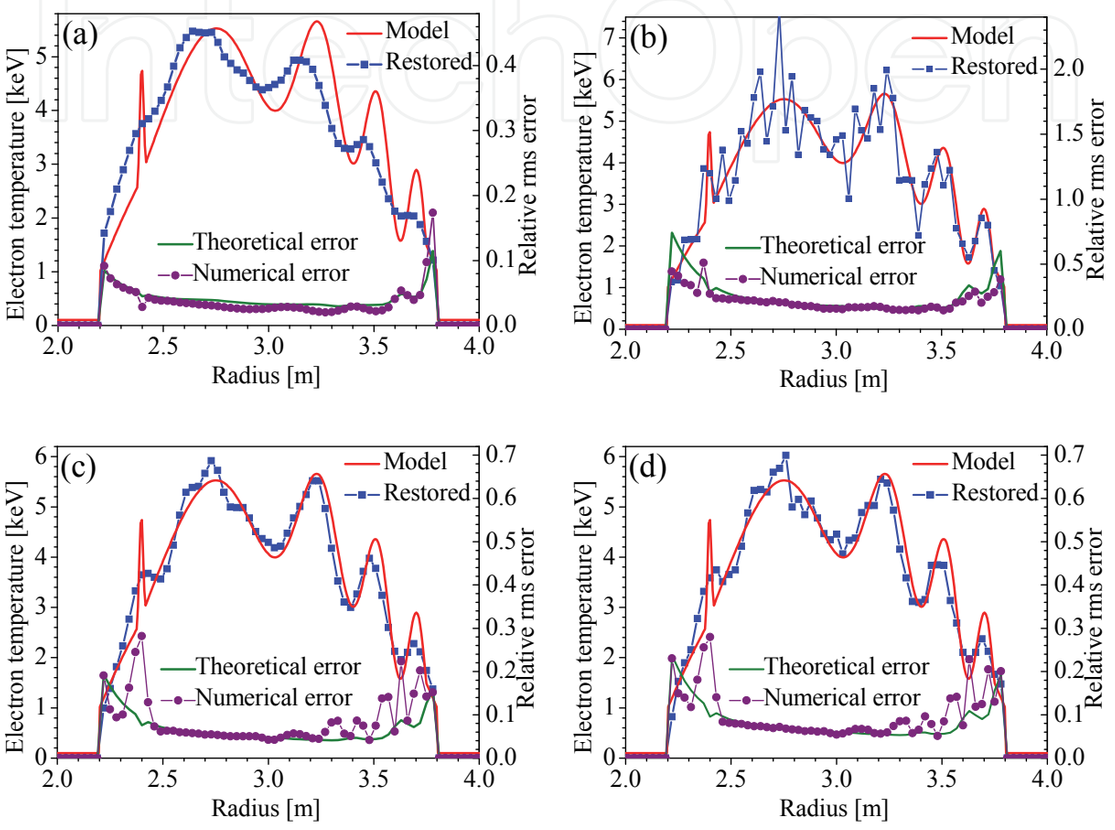

Fig. 13. Electron temperature profiles restored on the basis of the convolved (a) and deconvolved lidar profiles without filtering (b), and on the basis of the deconvolved lidar profiles smoothed by a monotone sharp-cutoff digital filter (with W=3cΔt_0/2) (c) and by a moving average filter (with W=2cΔt_0/2) (d); the right-hand y axis represents the theoretically estimated relative rms errors compared to the numerically obtained ones; n_e = 9x10^{19} m^{-3}.

The results of applying the deconvolution approach in the case of increased sensing pulse energy (E_0=3 J) are shown in Fig.14, where it is seen that the restoration accuracy is higher due to the higher SNR. This allows one to detect reliably smaller-scale inhomogeneities of the finer structure of the electron temperature profiles. In general, the increase of SNR, due for instance to increasing the electron concentration, the sensing pulse energy or the sensitivity of the photodetectors, is determinant for achieving high retrieval accuracy and resolution.

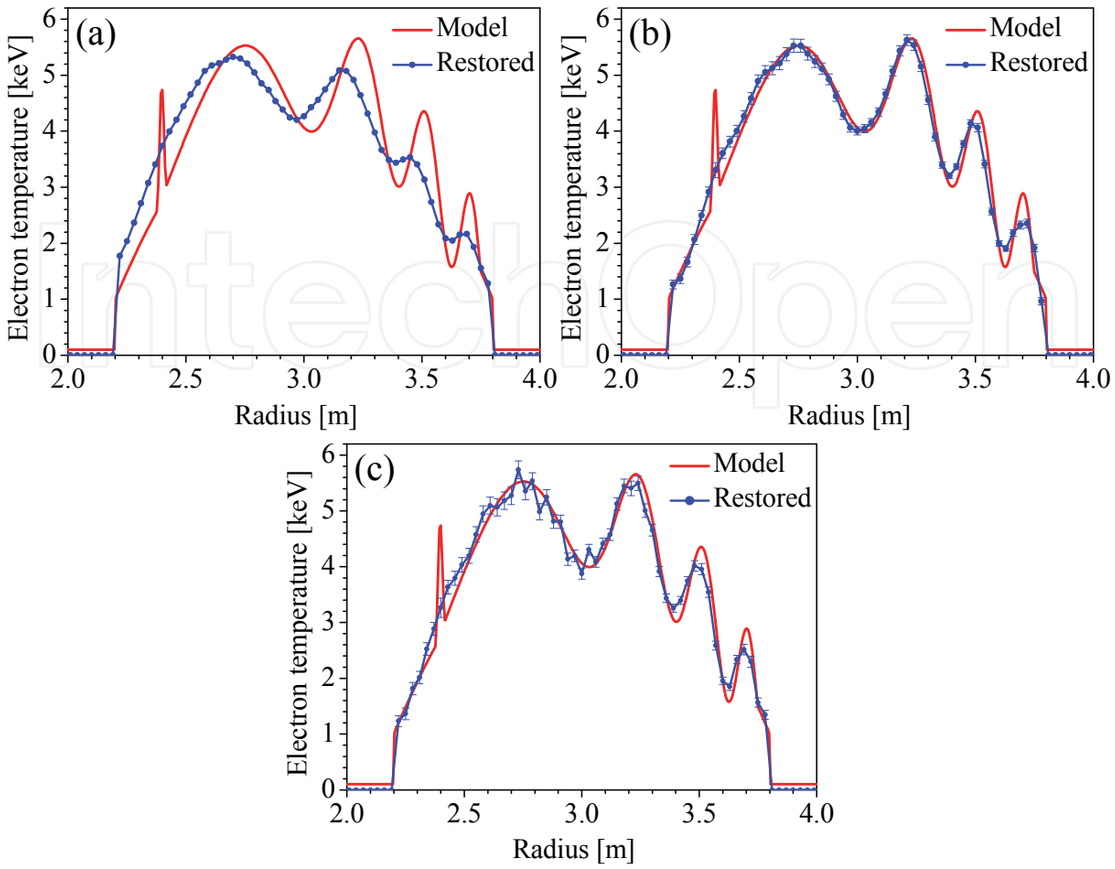

Fig. 14. Electron temperature profiles restored on the basis of the convolved (a) and deconvolved lidar profiles smoothed by a monotone sharp-cutoff digital filter (with $W=3c\Delta t_0/2$) (b) and by a moving average filter (with $W=2c\Delta t_0/2$) (c); $n_e=9\text{x}10^{19}$ m^{-3}, $E_0=3$ J. The statistical error represented by error bars, (b) and (c), is estimated on the basis of Eq.(54).

5. Conclusions

In the present chapter, the advantages and limitations have been considered of deconvolution techniques for improving the accuracy and resolution of the remote sensing of atmosphere, thermonuclear plasmas, and other objects by lidars of relatively long pulse response function including the laser pulse shape. Analog and photon counting modes of direct signal detection have been concerned. The general Fourier and Volterra deconvolution algorithms have been analyzed as well as some simple and fast special algorithms for the cases of rectangular, rectangular-like and exponentially-shaped pulse response functions. At negligible noise level, a high accuracy of recovering the short-pulse lidar profile is achievable at sufficiently short computing step. Also, by using suitable approaches, in some cases one can reduce the characteristic retrieval distortions due to some pulse response uncertainties. The strong broadband noise effect on the retrieval accuracy and resolution is revealed, including the noise accumulation with the distance of sensing for the recurrence algorithms. The noise influence in this case is shown to be effectively reduced by using appropriate compromise filtering or choice of the computing

step. That is, to avoid retrieval distortions, the filter window or the computing step should exceed the noise correlation radius (or time) but be less than the least variation (spatial or temporal) scale of the short-pulse lidar profile. The deconvolution procedures are shown as well to decrease the disturbing effect of narrow-band noise whose correlation time exceeds the pulse duration. Let us also underline the fact that the deconvolution-based retrieval of the short-pulse lidar profiles allows high-resolution sensing of small finite-size objects by longer laser pulses, realizing in this way double-sided linear-strategy optical tomography of such objects.

The investigations performed show as well that Fourier-deconvolution procedures, combined with appropriate low-pass filtering, applied to the measured Thomson scattering lidar profiles lead to several (2-3) times better resolution of recovering electron temperature profiles in fusion plasma, under conditions of plasma light background and amplification-enhanced Poisson noise. The convolution-due systematic errors are essentially corrected for and an acceptable restoration accuracy is achieved allowing one to reveal characteristic inhomogeneities in the distribution of the electron temperature within the plasma torus. It is also shown that, naturally, because of higher signal-to-noise ratio (stronger lidar return) the deconvolution accuracy increases with the increase of the electron concentration and the sensing pulse energy. This means that the deconvolution approach would be especially appropriate for processing data from a new generation of fusion reactors, such as ITER and DEMO, characterized by considerably higher electron concentration and sensing pulse energy compared to these achievable in JET.

6. Acknowledgments

This results described in the chapter was funded partly by the Bulgarian National Science Fund under Projects Ph-447, Ph-1511, and DO 02-107/2009 and the European Communities under the Contract of Association between EURATOM and INRNE (Bulgaria). This work was carried out in part within the framework of the European Fusion Development Agreement. The views and opinions expressed herein do not necessarily reflect those of the European Commission.

7. References

Bahrampour, A.R. & Askari, A.A. (2006). Fourier-Wavelet Regularized Deconvolution (ForWaRD) for Lidar Systems Based on TEA–CO2 laser, *Opt. Commun.*, vol. 257, pp. 97–111.

Brusaard, P.J. & van de Hulst, H.C. (1962). Approximation Formulas for Nonrelativistic Bremsstrahlung and Average Gaunt Factors for a Maxwellian Electron Gas, *Rev. Mod. Phys.*, vol. 34, pp. 507-520.

Casci, F.; Lanzinger, D. & Buceti, G., Eds. (2002). The Joint European Torus - a European Success Story, EFDA Close Support Unit, Culham, Available from http://www.jet.efda.org/wp-content/uploads/jeteuropeansucess.pdf

Dong, J.; Deng, P.; Liu, Y.; Zhang, Y.; Xu, J.; Chen, W & Xie, X. (2001). Passively Q-switched Yb:YAG Laser with Cr4+:YAG as the Saturable Absorber, *Appl. Opt.*, vol. 40, pp. 4303-4307.

Doviak, R.J. & Zrnic, D.S. (1984). *Doppler Radar and Weather Observation,* Academic Press, San Diego, USA.

Dreischuh, T.N.; Gurdev, L.L. & Stoyanov, D.V. (1995). Effect of Pulse-Shape Uncertainty on the Accuracy of Deconvolved Lidar Profiles, *J. Opt. Soc. Am. A*, vol.12, pp.301-306.

Dreischuh, T.N.; Gurdev, L.L. & Stoyanov, D.V. (1996). Lidar Profile Deconvolution Algorithms for Some Rectangular-Like Laser Pulse Shapes, In: *Advances in Atmospheric Remote Sensing with Lidar,* A.Ansmann, R. Neuber, P.Raioux, U. Wandinger, (Eds.), 135-138, Springer Verlag, ISBN 3540618872, Berlin.

Dreischuh, T.N.; Gurdev, L.L.; Stoyanov, D.V.; Protochristov, C.N. & Vankov, O.I. (2007). Application of a Lidar-Type Gamma-Ray Tomography Approach for Detection and Identification of Buried Plastic Landmines, *Proc. SPIE*, vol.6604, paper #660420.

Dreischuh, T.; Gurdev, L.; Stoyanov, D.; Beurskens, M.; Walsh, M. & Capel, A. (2009). Statistical Modeling of the Error in the Determination of the Electron Temperature in JET by a Novel Thomson Scattering LIDAR Approach, In: Proc. 36th EPS Conference on Plasma Physics. Contributed papers, *ECA*, vol.33E, P-2.149, European Physical Society, ISBN:2-914771-61-4, Geneva.

Dreischuh, T.; Gurdev, L. & Stoyanov, D. (2011). Statistical Modeling of Deconvolution Procedures for Improving the Resolution of Measuring Electron Temperature Profiles in Tokamak Plasmas by Thomson Scattering Lidar, *Proc. SPIE*, vol. 7747, paper # 77470T.

Foord, M. E.; Marmar, E. S. & Terry, J. L. (1982). Multichannel Light Detector System for Visible Continuum Measurement on Alcator C, *Rev. Sci. Instrum*., vol. 53, pp. 1407-1409.

Gurdev, L.L.; Dreischuh, T.N. & Stoyanov, D.V. (1993). Deconvolution Techniques for Improving the Resolution of Long-Pulse Lidars, *J. Opt. Soc. Am. A*, vol.10, No.11, pp. 2296-2306.

Gurdev, L.L.; Dreischuh, T.N. & Stoyanov, D.V. (1996). Deconvolution Algorithms for Improving the Resolution of Exponential-Shape Pulse Lidars", *Proc.SPIE*, vol. 3052, pp. 310-315.

Gurdev, L.L.; Dreischuh, T.N. & Stoyanov, D.V. (1998). Pulse Backscattering Tomography Based on Lidar Principle, *Opt. Commun*., vol. 151, pp. 339-352.

Gurdev, L.L.; Dreischuh, T.N. & Stoyanov, D.V. (2001). High-Resolution Doppler-Velocity Estimation Techniques for Processing of Coherent Heterodyne Pulsed Lidar Data, *J. Opt. Soc. Am. A*, vol. 18, pp.134-142.

Gurdev, L.L.; Dreischuh, T.N. & Stoyanov, D.V. (2002). High Range Resolution Velocity Estimation Techniques for Coherent Doppler Lidars with Exponentially-Shaped Laser Pulses, *Appl. Opt.*, vol. 41, pp. 1741-1749.

Gurdev, L.L. & Dreischuh, T.N. (2003). High Range Resolution Velocity Estimation Techniques taking into Account the Frequency Chirp in Coherent Doppler Lidars, *Opt. Commun.,* vol. 219, pp.101-116.

Gurdev, L.L.; Stoyanov, D.V.; Dreischuh, T.N.; Protochristov, C.N. & Vankov, O.I. (2007a). Gamma-Ray Backscattering Tomography Approach Based on the Lidar Principle, *IEEE Transactions on Nuclear Science,* vol. 54, No.1, part 2, pp.262-275.

Gurdev, L.L.; Dreischuh, T.N.; Stoyanov, D.V. & Protochristov, C.N. (2007b). Gamma-Ray Lidar (GRAYDAR) in-Depth Sensing of Optically Opaque Media, In: *Nuclear*

Methods for Non-Nuclear Applications, Ch. Stoyanov, (Ed.), Heron Press, ISBN: 978-954-580-209-6, Sofia.

Gurdev, L.L. & Dreischuh, T.N. (2008a). On an approach for improving the range resolution of pulsed coherent Doppler lidars, *J. Mod. Optics*, vol. 55, No.9, pp.1441-1462.

Gurdev, L.L.; Dreischuh, T.N. & Stoyanov, D.V. (2008b). Potential Accuracies of Some New Approaches for Determination by Thomson Scattering Lidar of the Electron Temperature Profiles in Thermonuclear Plasmas, *Proc. SPIE*, vol. 7027, # 702711.

Hannon, S.M. & Thomson, J.A. (1994). Aircraft Wake Vortex Detection and Measurement with Pulsed Solid-State Coherent Laser Radar, *J. Mod. Optics*, vol. 41, pp.2175–2196.

Johnstone, I.; Kerkyacharian, G.; Picard, D., & Raimondo, M (2004). Wavelet Deconvolution in a Periodic Setting, *J. Roy. Stat. Soc. B,* vol. 66, pp. 547–573, with discussion on pp. 627-652.

Kempenaars, M.; Flanagan, J. C.; Giudicotti, L.; Walsh, M. J.; Beurskens, M. & Balboa, I. (2008). Enhancement of the JET Edge LIDAR Thomson Scattering Diagnostic with Ultrafast Detectors, *Rev. Sci. Instrum.*, vol. 79, 10E728.

Kempenaars, M.; Balboa, I.; Beurskens, M.; Flanagan, J. C. & Maslov, M. (2010). The JET Core LIDAR Diagnostic, Int. Conference on Plasma Diagnostics, Pont-à-Mousson, France, 12-16 April 2010, paper P30.

Kondoh, T.; Lee, S.; Hutchinson, D. P. & Richards, R. (2001). Collective Thomson Scattering Using a Pulsed CO2 Laser in JT-60U, *Rev. Sci. Instrum.*, vol. 72, pp. 1143-1146.

Kovalev, V.A. & Eichinger, W.E. (2004). *Elastic Lidar: Theory, Practice, and Analysis Methods*, Wiley, New York, USA.

Marzano, F.S. & Visconti, G., Eds. (2002). *Remote Sensing of Atmosphere and Ocean from Space: Models, Instruments and Techniques*, Kluwer Academic Publishers, Dodrecht.

Measures, R.M. (1984). *Laser Remote Sensing*, Wiley, New York, USA.

Naito, O.; Yoshida, H. & Matoba, T. (1993). Analytic Formula for Fully Relativistic Thomson Scattering Spectrum, *Phys. Fluids B*, vol. 5, pp. 4256-4258.

Park, Y. J.; Dho, S.W. & Kong, H.J. (1997). Deconvolution of Long-Pulse Lidar Signals with Matrix Formulation, *Appl. Opt.*, vol. 36, pp. 5158-5161.

Pensky, M. & Sapatinas, T. (2009). Functional Deconvolution in a Periodic Setting: Uniform Case, *Ann. Statist.*, vol. 37, pp. 73-104.

Pensky, M. & Sapatinas, T. (2010). On Convergence Rates Equivalency and Sampling Strategies in Functional Deconvolution models, *Ann. Statist.*, vol. 38, pp. 1793-1844.

Refaat, T.F.; Ismail, S.; Abedin, M. N.; Spuler, S.M. & Singh, U. N. (2008). Lidar Backscatter Signal Recovery from Phototransistor Systematic Effect by Deconvolution, *Appl. Opt.*, vol. 47, No. 29, pp. 5281-5295.

Rytov, S.M. (1976). *Introduction to Statistical Radiophysics,* vol. 1, Nauka, Moscow.

Salzmann, H. et al., (1988). The LIDAR Thomson Scattering Diagnostic on JET, *Rev. Sci. Instrum.*, vol. 59, pp. 1451-1456.

Sheffield, J. (1975). *Plasma Scattering of Electromagnetic Radiation*, Academic, New York.

Stoyanov, D.V.; Gurdev, L.L. & Dreischuh, T.N. (1996). Reduction of the Pulse Spike Cut Error in Fourier-Deconvolved Lidar Profiles, *Appl. Opt.*, vol.35, pp.4798-4802.

Stoyanov, D.V.; Gurdev, L.L.; Kolarov, G.V. & Vankov, O.I. (2000). Lidar Profiling by Long Rectangular-Like Chopped Laser Pulses, *Opt. Engineering*, vol. 39, pp. 1556-1567.

Stoyanov, D.V.; Dreischuh, T.N.; Vankov, O.I. & Gurdev, L.L. (2004). Measuring the Shape of Randomly Arriving Pulses Shorter than the Acquisition Step, *Meas. Sci. Technol.*, vol. 15, pp.2361-2369.

Stoyanov, D.; Nedkov, I. & Ausloos, M. (2007). Retrieving True Images through fine grid steps for enhancing the resolution beyond the classical limits: theory and simulations, *Journal of Microscopy*, vol. 226, pp. 270–283.

Stoyanov, D.; Dreischuh, T.; Gurdev, L.; Beurskens, M.; Ford, O.; Flanagan, J.; Kempenaars, M.; Balboa, I. & Walsh, M. (2009). Deconvolution of JET Core LIDAR data and Pedestal Detection in Retrieved Electron Temperature and Density Profiles, In: Proc. 36th EPS Conference on Plasma Physics. Contributed papers, *ECA*, vol.33E, P-2.155, European Physical Society, ISBN:2-914771-61-4, Geneva.

Stoyanov, D.; Beurskens, M.; Dreischuh, T.; Gurdev, L.; Ford, O.; Flanagan, J.; Kempenaars, M.; Balboa, I. & Walsh, M. (2010). Resolving the Plasma Electron Temperature Pedestal in JET from Thomson Scattering Core LIDAR Data, In: Proc. 37th EPS Conference on Plasma Physics. Contributed papers, *ECA*, vol.34A, P5.133 European Physical Society, ISBN 2-914771-62-2, Geneva.

Van Trees, H.L. (2001). *Detection, Estimation, and Modulation Theory, Part III, Radar-Sonar Signal Processing and Gaussian Signals in Noise*, Wiley, New York, USA.

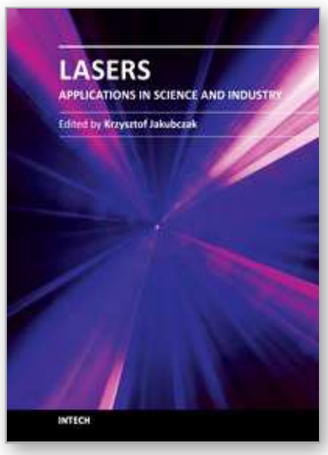

Lasers - Applications in Science and Industry
Edited by Dr Krzysztof Jakubczak

ISBN 978-953-307-755-0
Hard cover, 276 pages
Publisher InTech
Published online 09, December, 2011
Published in print edition December, 2011

The book starts with basic overview of physical phenomena on laser-matter interaction. Then it is followed by presentation of a number of laser applications in the nano-particles and thin films production, materials examination for industry, biological applications (in-vitro fertilization,tissue ablation) and long-range detection issues by LIDARs.

How to reference
In order to correctly reference this scholarly work, feel free to copy and paste the following:

Ljuan L. Gurdev, Tanja N. Dreischuh and Dimitar V. Stoyanov (2011). Deconvolution of Long-Pulse Lidar Profiles, Lasers - Applications in Science and Industry, Dr Krzysztof Jakubczak (Ed.), ISBN: 978-953-307-755-0, InTech, Available from: http://www.intechopen.com/books/lasers-applications-in-science-and-industry/deconvolution-of-long-pulse-lidar-profiles

INTECH
open science | open minds

InTech Europe
University Campus STeP Ri
Slavka Krautzeka 83/A
51000 Rijeka, Croatia
Phone: +385 (51) 770 447
Fax: +385 (51) 686 166
www.intechopen.com

InTech China
Unit 405, Office Block, Hotel Equatorial Shanghai
No.65, Yan An Road (West), Shanghai, 200040, China
中国上海市延安西路65号上海国际贵都大饭店办公楼405单元
Phone: +86-21-62489820
Fax: +86-21-62489821

IntechOpen